Ph.D. Dissertation of

Biofabrication of a scaffold-free 3D cardiac tissue construct: a promising *ex vivo* model for *in situ* detection of drug-induced Na^+/K^+ ion channel responses

스캐폴드가 없는 3D 심장 조직 구조물의 생체 제작: 약물 유도된 나트륨/칼륨 이온채널 반응의 현장 검출을 위한 유망한 생체 외 모델

August 2023

Graduate School of Pharmacy
Seoul National University
Pharmaceutical Science Major

Samson Annie Agnes Suganya

Biofabrication of a scaffold-free 3D cardiac tissue construct: a promising *ex vivo* model for *in situ* detection of drug-induced Na^+/K^+ ion channel responses

Under the guidance of Professor Joon Myong Song

Submitting a Ph.D. Dissertation of Pharmacy

August 2023

Graduate School of Pharmacy
Seoul National University
Pharmaceutical Science Major

Samson Annie Agnes Suganya

Confirming the Ph.D. Dissertation written by
Samson Annie Agnes Suganya
August 2023

Chair	김 대 덕	(Seal)
Vice Chair	창 동 신	(Seal)
Examiner	송 준 명	(Seal)
Examiner	정 아 람	(Seal)
Examiner	강 윤 표	(Seal)

Abstract

Current drug discovery is hampered by inadequate models that do not accurately reflect physiological responses to treatment. Several drugs have recently been withdrawn from the market because of lack of efficacy or because of unexpected side effects, especially cardiotoxicity, that were not detected during clinical trials. The main objective of this dissertation is to develop a scaffold-free 3D-printed (SFP) biomimetic cardiac tissue construct to study drug-induced blockage of sodium and potassium ion channels. In this work, a 3D printing technology called scaffold-free 3D-printed (SFP) model was used to rapidly and spatially arrange rat embryonic cardiomyocytes (H9C2) in hydrogels. By varying the formulation of the bioink and embedding the cardiomyocytes in a specific microarchitecture, the cardiomyocytes preferentially aligned with the designed geometry and regenerated as biomimetic cardiac tissue with a branched cell structure with multinucleated cells resembling the native tissue-like phenotype. The SFP-engineered 3D cardiac cells achieved high confluence with a branched cell structure with multiple nuclei. The formation of tight intracellular junctions expressing connexin 43 confirmed the maturation of the fabricated structure. Using this approach, cardiac tissue constructs were successfully fabricated and used as an assay platform sensitive enough to measure sodium and potassium ion channel responses.

Initially, this study focused on in situ measurement of physiological sodium and potassium ion channel responses of the bioengineered cardiac construct to known cardiac drugs. By using various small molecules, it was demonstrated that SFP-engineered 3D cardiac tissue constructs can be used for screening and drug discovery due

to their high predictability of drug response in vitro. Next, we investigated the sensitivity of SFP-engineered 3D cardiac tissue constructs for screening size-dependent blockade of the human ether-à-go-go-related (hERG) gene potassium channel by nanomaterials. To achieve this goal, gold nanoparticles with different size and surface ligand were synthesized, and their size- and surface ligand-dependent blockade of the hERG potassium channel was uniquely measured by monitoring potassium ion channel permeability and hERG protein immunofluorescence using 3D biomimetic cardiac tissue models. Our results suggest that the proposed SFP-based bioprinted 3D constructs of the heart, which allow fluorescence-based measurement of the membrane potential of sodium and potassium ion channels, can be used as a screening tool to measure the blockade of ion channels by nanomaterials down to small molecules.

Keyword : 3D bioprinting, hERG potassium channel, nanoparticle, cardiotoxicity, drug screening

Student Number : 2017-31026

Table of Contents

Introduction

1.1 Three-dimensional bioprinting

Bioprinting enables the transfer of non-living materials such as proteins, drugs, biomaterials, ECM components, and living cells onto solid, gel, or liquid media with predetermined and precise spatial positions [1]. Two-dimensional (2D) bioprinting was first reported in the late 1980s when a modified office inkjet printer was used to deposit cell adhesion proteins in predefined positions on substrates [2]. In 2003, Wilson and Boland used this technology to print viable cells for the first time [3]. But the researchers did not limit themselves to 2D patterning. In 2004, Smith et al. applied cell extrusion for the first time to deposit viable cells in 3D [4]. Extrusion-based bioprinting systems use a continuous flow of biomaterials to produce tissue constructs. A set of motors or magnetic rails with coordinates set by computer-aided designs (CAD) position a nozzle or the stage in a specific location along with pressure or flow rates to dispense materials at a specific time. Typically, materials are dispensed by pressure or mechanically (plunger or screw) [5]. Pure biomaterial or biomaterials loaded with cells can be printed layer by layer on a substrate. Usually, different hydrogels are used for extrusion in bioprinters. Depending on the material used, the hydrogels can be cross-linked either physically (i.e., by ionic or thermal crosslinking) or chemically [6-8]. Recent advances in 3D bioprinting techniques have demonstrated that cardiac tissue engineering technology can be used for drug screening and in vitro disease modeling. 3D printing-based bioengineering has the potential to develop functional tissue constructs that replace the need for native tissue. In general, tissue

engineering uses materials such as viable cells, biomaterials (Matrigel, collagen, fibrin, hyaluronic acid, PCL, PLGA, PLA, etc.), and extracellular matrix (ECM) components to create functional tissue constructs [9–13]. Although bioengineered cardiac tissue constructs can be an effective tool to study cardiac function, the artificial substitutes are limited in their ability to produce well-defined structural and functional properties that resemble natural cardiac tissue. This limits their wide range of applications.

1.2 Biomaterials for 3D printing

The choice of an appropriate biomaterial is important to print and develop cardiac tissue. It must mimic the biochemical and mechanical properties of the native extracellular matrix. In the context of 3D bioprinting, various mechanisms have been used to print both naturally derived and synthetic hydrogel precursors. Regardless of the biomaterial selected, the biomaterials must be able to rapidly form a hydrogel network during the printing process through either chemical or physical crosslinking mechanisms. Commonly used natural biomaterials for cardiac tissue engineering include extracellular matrix proteins such as fibrin [14], collagen [15], gelatin [16], and decellularized cardiac matrix [17,18].

1.3 Current State-of-the-Art 3D-Printed Cardiac Models

Most of the work to develop these platforms for drug discovery and screening and physiological modeling has focused on replicating micro-tissues of the left ventricular myocardium, the site of the most severe heart disease. These micro-tissues are generally created by seeding cells on or encapsulating cells in a structured scaffold that mimics the extracellular matrix to guide and support tissue growth

[19]. Several groups have been working on 3D-printed heart models. However, research on these models is still in the early stages of development. Thus, Jang et al developed a 3D stem cell patch with prevascularized cells using decellularized extracellular matrix from cardiac tissue (hdECM) as a bioink. The reported stem cell patch promoted intercellular interaction and stem cell differentiation, thus improving therapeutic efficacy in cardiac repair [20]. Similarly, Park et al. showed that dual stem cell therapy using cardiomyocytes derived from human induced pluripotent stem cells (hiPSC-CMs) and a patch loaded with human mesenchymal stem cells (hMSC- PA) synergistically improved cardiac function in a rat myocardial infarction model [21]. On the other hand, Das et al. reported the effect of decellularized ECM biotin and external stimuli on cardiac tissue development. The authors observed a difference in cardiomyocyte behavior depending on the composition of the biotin and the culture conditions [22].

Beauchamp et al. reported that scaffold-free multicellular cardiac spheroids were developed that could contract spontaneously and synchronously. While cardiac spheroids have played an important role in drug testing and are widely used due to their ease of fabrication, these constructs lack the physiological properties of cardiac muscle that are critical for maintaining the long-term functionality of artificial cardiac tissues [23-26]. However, scaffold-based techniques offer other advantages. The architecture of the scaffolds can be conveniently modulated to promote the biological relevance of the artificial tissues by adjusting the spatial organization to mimic their respective counterparts in vivo.

Previous strategies for generating 3D cardiac tissue were based on printing cells (hydrogel-embedded cells) into prefabricated scaffolds (accordion-like honeycomb structure, microfluidic bioreactor, microfilament arrays, biowire approach, polymer-based pillar structures, or hydrogel patches). However, these scaffold-based printing methods suffer from inhomogeneous structure formation (example: Cardiac cells grow as multicellular spheroids instead of elongated structures), inconsistent reproducibility, and lack of precise control over key scaffold parameters. In general, native myocardial tissues are organized into parallel cardiac fibers with aligned intracellular contractile myofibrils and gap junction complexes between contacting cardiomyocytes, which are important for forming the integrated electrical and mechanical properties of the heart. When cardiac cells are printed based on prefabricated scaffold patterns, inconsistent performance and inhomogeneous structure formation may occur. The capabilities of 3D printing of cardiac tissue are currently limited and the development of new models to better assess tissue function and disease progression is very promising.

1.4 Role of voltage-gated ion channels in drug screening

In the heart, prominent voltage-gated ion channels include sodium (Na^+), potassium (K^+) and calcium (Ca^{2+}) channels, and their inhibition by drugs can to lead to serious adverse effects. The human ether-a-go-go-related gene (hERG) encodes the tetrameric potassium channel $K_v11.1$. This hERG K^+ channel conducts the rapid component of the delayed rectifier K^+ current in the heart (I_{Kr}). Inhibition of the hERG channel may result in long QT syndrome

(LQTS) and cause severe cardiac arrhythmia [27-30]. Adverse drug-induced blockade of the hERG K^+ channel may therefore lead to failure of drug development and be a reason for withdrawal of the drug from the market [31-33]. Structural data has verified that the key aromatic residues in the S6 helix (Tyr-652, Phe-656) and the pore helix (Thr-623, Ser-624, Val-625) of the $K_v11.1$ channel are detrimental targets of compounds that impair K^+ ion flux through the pore and therefore reduce I_{Kr}.

1.5 3D bioprinted cardiac constructs for drug screening

It is important to evaluate chemical blockade of the hERG channel at an early stage of drug development. To this end, several in vitro methods have been developed, including rubidium flux assays, radioligand binding assays, electrophysiological measurements, and fluorescence-based assays [34-36]. 2D cell-based screening assays are commonly performed to evaluate new drug candidates in the early stages. Although 2D *in vitro* cell models offer high-throughput capability, they often give false predictions because of the over-simplified cell microenvironment [37-39]. As mentioned before, 3D cell culture methods based on bioprinting have been shown to be superior to conventional 2D cell culture methods commonly used in research laboratories. In 2D cell culture, the cellular morphology differs from that of natural tissue due to the additional surface tension and one-sided cell adhesion in the cell culture flask. The advantages of 3D bioprinting lie in its ability to produce functional tissues/organs that exhibit dynamic properties to mimic native tissues. Because bioengineered tissue constructs can mimic native tissue structures, they can be used directly for drug screening studies without the need

to detach or isolate the tissue construct and its cells from the hydrogel.

1.6 Interaction of Nanomaterials with ion channels

Multifunctional nanomaterials have received considerable attention for their potential to enhance antitumor activity and reduce toxicity. Gold nanoparticles (AuNPs) are attractive nanomaterials that possess multifunctional anti-cancer activities due to a variety of surface chemistries [40,41]. Due to their size- and shape-dependent optoelectronic properties, easy surface functionalization, biocompatibility, and low toxicity, AuNPs have been used in various biomedical fields, including photothermal therapy (PTT) [42], contrast agents for bioimaging [43,44], therapeutic agents [45-47], radiosensitizers [48], and gene transfection agents [49]. In particular, the ease of functionalization with active ligands via Au-S chemical bonds makes AuNPs reliable drug carriers when used in conjunction with PTT [50]. As a result, various multifunctional AuNPs with drug carrier function have been prepared based on surface modifications, such as conjugation with polyethylene glycol (PEG), for cancer theranostics [41,51]. So far, established in vitro cytotoxicity assays have shown that AuNPs are not toxic [52]. However, when different cap molecules are used to synthesize AuNPs, they may induce toxic properties, such as oxidative stress, depending on the materials applied on them [53]. Due to their particular molecular architecture and accessible location, ion channels are potential targets for synthetic drugs and biomaterials such as surface functionalized AuNPs. Triphenylphosphine (TPP)-stabilized AuNPs have been reported to irreversibly block the permeability of K^+ channels in 2D cell cultures, whereas thiol-stabilized AuNPs of similar size showed

no such effect in vitro [54]. Therefore, the potential hazards of surface-functionalized AuNPs are an important issue that should be further investigated. In particular, for the successful development of nanomaterials, it must be demonstrated that anticancer drugs conjugated to the surface of AuNPs do not block the hERG potassium channel. Size-dependent blockade of the hERG potassium channel is another factor that needs to be considered with respect to nanomaterials, as inhibition of K^+ permeation in K^+ channels may occur in a size-dependent manner due to the binding of nanomaterials to hERG proteins.

1.7 A fluorescence-based in situ measurements

A simple fluorescence-based assessment of membrane potential can be readily applied to the bioprinted construct, assessing the overall tissue response to the drug. Isolation of the tissue construct and its cells from the hydrogel requires additional performance, which may damage the tissue construct during the process. Therefore, simple fluorescence-based in situ detection of physiological sodium and potassium ion channel responses using a 3D bioprinting platform may be beneficial. Because bioprinted gels cannot be used directly for patch clamp or microelectrode array measurements, fluorescent dye-based assessment of membrane potential without isolation of the tissue construct from the hydrogel may be considered as an option for measuring drug-induced sodium and potassium channel blockage of printed cardiac cells. In this work, a scaffold-free printing (SFP) method with precise printing patterns was used to generate stable cardiac tissue constructs. In the developed method, cells were trapped between the 3D printed cell-loaded patterns during printing. Since the hydrogel composition is more rigid, the

original printed shape was maintained after printing. The SFP-based 3D printed construct provided the necessary space for the printed cells to grow and proliferate. In addition, for the first time an in situ measurement to screen the blockage of ion channels caused by nanomaterials was demonstrated. The developed 3D cardiac tissue construct was used for high-throughput drug screening. The work in this dissertation could lay the foundation for the development of future disease and drug screening models.

The Research Aim and Objectives

The aimed objective of this doctoral dissertation includes development and verification of nanomaterial-induced size-dependent hERG gene potassium channel block using an *in-situ* enabled 3D bioengineered cardiac tissue model.

The objectives of the doctoral dissertation consist of:

a. Chemical synthesis of multifunctional anticancer spherical gold nanoparticles whose surface was bound with the ligand of thiol-terminated polyethylene glycol (PEG) conjugated to indomethacin (IMC-PEG-SH@AuNPs). Chemical synthesis of Triphenylphosphine-stabilized gold nanoparticles (F-108@TPP-AuNPs).
b. Implementation of biomimetic 3D cardiac constructs as a drug screening platform to evaluate nanomaterial-induced hERG potassium channel blockage.
c. Studied small-molecule-induced hERG K^+ channel block using 3D bioengineered cardiac construct.
d. Studied nanomaterial-induced hERG K^+ channel block using 3D bioengineered cardiac constructs
e. Implementation of 3D bioprinted cardiac constructs to verify size-dependent effect of the nanomaterials on the hERG K^+ channel block.

Each of these objectives has been thoroughly investigated and the author's research activity has resulted in scientific contributions.

Experimental Methods and Materials

3.1 Materials and methods

All chemicals and solvents used for synthesis were purchased from Sigma-Aldrich or Alfa-Korea and used as such without further purification. Moisture sensitive reactions were generally carried out under argon or nitrogen gas. Column chromatography was carried out in silica gel (Merck, silica gel 60, particle size 0.063-0.200 mm, 70-230 mesh ASTM) using the commercial grade solvent as the mobile phase. The progress of all reactions was monitored by TLC, which was performed on 2.0 × 4.0 cm^2 aluminum sheets precoated with silica gel 60 (HF-254, Merck) to a thickness of 0.25 mm. The developed chromatograms were viewed under ultraviolet light (254 and 365 nm). ^{1}H and ^{13}C NMR spectra were recorded in deuterated chloroform or dimethyl sulfoxide (Cambridge Isotope Labs) containing 1 % TMS as an internal standard, and Bruker AVANCE600 and AVANCE400 spectrometers were used. Chemical shifts are reported in values (ppm) relative to the internal TMS, and J values are reported in Hz. The abbreviations for the peak multiplicities are as follows: s (singlet), d (doublet), dd (doublet of doublets), t (triplet), q (quartet), m (multiplet), and br (broad). ESI-MS was obtained with an Agilent 6530 Q-TOF LC-MS spectrometer.

3.2 Synthesis of IMC-PEG-SH (4)

Intermediate **1** was synthesized *via* the amidation of 1-(4-chlorobenzoyl)-5-methoxy-2-methyl-3-indoleacetic acid (IMC) and *tert*-butyl *N*-(2-aminoethyl)carbamate in the presence of EDC•HCl/HOBt (EDC = 1-(3-dimethylaminopropyl)-3-ethylcarbodiimide hydrochloride; HOBt, 1-hydroxybenzotriazole

hydrate; TEA, triethylamine) to afford *tert*-butyl (2-(2-(1-(4-chlorobenzoyl)-5-methoxy-2-methyl-1*H*-indol-3-yl)acetamido)ethyl)carbamate (1). Subsequently, *tert*-butyl deprotection using a solution of HCl (4 M) in anhydrous dioxane at 25 ° C afforded intermediate **2.** Then, acid-amine coupling of intermediate **2** and 2-oxo-6,9,12,15,18,21,24,27-octaoxa-3-thiatriacontan-30-oic acid (**6**) resulted in the formation of compound **3** in good yield. Compound (**6**) was synthesized by protecting 1-mercapto-3,6,9,12,15,18,21,24-octaoxaheptacosan-27-oic acid (**5**) at the thiol end using $(CH_3CO)_2O$ in the presence of a catalytic amount of DMAP in acetonitrile at 0 ° C. Finally, the deprotection of compound **3** was achieved using a solution of HCl (1 M) in anhydrous dioxane to afford *N*-(2-(2-(1-(4-chlorobenzoyl)-5-methoxy-2-methyl-1*H*-indol-3-yl) acetamido) ethyl)-1-mercapto-3,6,9,12,15,18,21,24-octaoxaheptacosan-27-amide **4** (IMC-PEG-SH) in moderate yield.

3.3 Synthesis of AuNPs

3.3.1 Preparation of 9-nm AuNPs

The AuNP solution was prepared using the standard sodium citrate reduction method, with some modifications [55]. Briefly, a solution of 2.2 mM sodium citrate dihydrate in Milli-Q water (150 mL) was heated in a 250-mL three-necked round-bottom flask for 15 min under vigorous stirring. After boiling, 1 mL of $HAuCl_4$ (25 mM) was quickly added to the flask. The color of the solution changed from yellow to bluish gray and then to deep red within a few minutes. The reaction mixture was boiled for another 30 min, and then mild stirring was applied until it cooled to room temperature. The products were

stored in a refrigerator at 4 ° C. The size of the AuNPs was determined by transmission electron microscopy (TEM).

3.3.2 Preparation of 17-nm AuNPs

Citrate-stabilized AuNPs (17 nm) were synthesized using a previously reported method, with some modifications [56]. Briefly, an aqueous solution of 0.3 mM $HAuCl_4 \cdot 3H_2O$ (50 mL) was boiled with vigorous stirring. To this solution, 5 mL of 10 mM sodium citrate solution was added. The mixture turned blue within 30 s and changed to red violet in 120 s. After boiling for 15 min, the heating source was removed and the colloid was stirred for another 20 min. The solution was then cooled to room temperature and stored in a refrigerator at 4 ° C. The size of the AuNPs was determined by TEM.

3.3.3 Preparation of 46-nm AuNPs

The 46-nm AuNPs were synthesized using a modified citrate reduction method that has been previously reported [57]. Briefly, a $HAuCl_4$ solution (0.3 mM × 78.4 mL) was added to boiling sodium citrate dihydrate solution (38.8 mM × 0.59 mL), and the reaction was allowed to proceed for 30 min. The synthesized AuNP solution was then cooled to room temperature and stored in a refrigerator at 4 ° C. The size of the AuNPs was determined by TEM.

3.4 Functionalization of AuNPs with thiol-terminated PEG-indomethacin (IMC-PEG-SH@ AuNP)

Citrate-coated AuNPs were functionalized using synthesized thiol ligands (IMC-PEG-SH) *via* a modified place-exchange reaction (Scheme S2). Briefly, an aqueous solution of IMC-PEG-SH-ligand

(10 mM) was added to 1 mL of each AuNP solution (Au_9NPs, Au_{17}NPs, and Au_{46}NPs), which were incubated for 24 h at 4 ° C. Then, the supernatant was removed by centrifugation and the modified AuNPs were washed and re-suspended in H_2O. The modified AuNPs were characterized by UV-Vis spectroscopy, dynamic light scattering (DLS), and ζ-potential measurements. Results are presented as mean ± standard deviation (SD).

3.5 Synthesis of F-108@TPP-AuNPs

Triphenylphosphine (TPP)-functionalized and F-108 pluronic polymer-stabilized gold nanoparticles (F-108@TPP-AuNPs) were synthesized according to a previously reported method [58] with some modifications. Briefly, TPP-Au(I)Cl (0.03 mmol) was dissolved and sonicated in a 35-mL vessel with a crimp cap containing 30 mL of 1% F-108 pluronic solution and 90 μL of 1 M NaOH (pH = 10.5). The mixture was heated via microwave irradiation in a microwave reactor. The power was modulated to reach 110 ° C, and the temperature was maintained for 25 min. A red solution was obtained, confirming the presence of 108@TPP-AuNPs. To ensure the purity of the F-108@TPP-AuNPs, the solution was dialyzed for 24 h to remove any remaining impurities and analyzed by energy-filtered transmission electron microscopy (EFTEM), UV-Vis spectroscopy, and ^{1}H NMR studies.

3.6 Characterization of nanoparticles

3.6.1 EFTEM

The diameters of the different-sized AuNPs were characterized using EFTEM. Nanoparticle samples were prepared on a holey carbon film mounted on a copper grid. A drop of diluted AuNP1/

AuNP2/ AuNP3/ F-108@TPP-AuNPs solution was spotted onto the grid and dried overnight at room temperature (298 K).

3.6.2 UV-Vis spectroscopy

The absorption spectra of the AuNPs were measured using an Evolution™ 60 UV-visible spectrophotometer (Thermo Fischer Scientific, USA). Quartz cuvettes with a thickness of 1 cm were used in the experiments. The as-synthesized AuNPs (unconjugated), IMC-PEG-SH@AuNPs (conjugated), and F-108@TPP-AuNPs were characterized using UV-Vis spectroscopy to confirm the formation and stability of AuNPs.

3.6.3 DLS and zeta-potential measurements

To measure the hydrodynamic size and zeta potential of AuNPs, DLS and zeta-potential measurements were conducted using a Zetasizer Nano ZS (Malvern Instruments Ltd., UK) equipped with a 633-nm laser. All measurements were equilibrated for 120 s in water at 25 ° C. In each measurement, the number of runs and the duration were set automatically.

3.7 Molecular docking

Molecular docking of IMC-PEG-SH and TPP into the three-dimensional X-ray crystal structure of the human ether-a-go-go related K^+ channel (PDB:5VA1) was carried out using the LibDock program (Discovery Studio 4.0). The 3D structures of IMC-PEG-SH and TPP were constructed using the Discovery Studio small-molecule window, and energy was minimized by the CHARMm force field with a minimum RMS gradient of 0.09. The 3D crystal structure of PDB5VA1 was retrieved from the RCSB Protein Data Bank

(http://www.rcsb.org/pdb/). Discovery Studio 4.0 uses a simulated annealing procedure to explore the binding possibilities of a ligand in a binding pocket. Before docking, all bound water molecules and heteroatoms were removed from the protein crystal structure. The structure of the hERG protein was used to dock IMC-PEG-SH and TPP. A CHARMm-based molecular dynamics scheme was used to identify the optimal binding sites for docking. The optimal binding site was chosen based on the shape and location of the cavity, location of the residue, and conserved amino acid. A site sphere radius was set to assign the entire binding pocket, and the other parameters were set to default. The most suitable compounds were ranked by the corresponding values of LibDock score, and all values were preserved to determine the most probable binding mode.

3.8 Cell culture

Rat embryonic cardiomyocytes (H9c2(2-1) cells) were purchased from the American Type Culture Collection (ATCC; Manassas, VA, USA; cat. no.: CRL-1446^{TM}). The cells were cultured in Dulbecco's modified Eagle's medium (DMEM; cat. no. BE12-604F, Lonzo Bio Whittaker) supplemented with 10% (v/v) fetal bovine serum (FBS; cat. no. 16000-044, GIBCO). Cells were grown in an atmosphere of 5% CO_2 at 37 ° C.

3.9 Bioink formulation for three-dimensional printing

Bioink was prepared by dissolving sodium alginate (SA) (cat. no. A2033, Sigma), gelatin (GEL) (cat.no. G1890, Sigma), and fibrinogen (Fg) (cat. no. F8630, Sigma) in 1× phosphate buffer saline (PBS). SA and GEL powders were dissolved at 80 ° C for 6 h and allowed to cool to room temperature. Fg solution was obtained by dissolving Fb powder in PBS at 37 ° C for 1 h, after which 50 U/mL aprotinin was

added to the Fg solution. Finally, a viscous hydrogel was obtained by adding the SA: GEL mixture to the Fg solution, and the bioink mixture was stirred until homogenous.

H9c2(2−1) Cells were trypsinized from the culture flasks, washed, and quantified. The cells were then mixed with sodium alginate (20 mg/mL), gelatin (60 mg/mL), and fibrinogen (30 mg/mL) hydrogel (SA: GEL: Fg) at a density of 5×10^6 cells/mL. After mixing, 1 mL of the mixture was loaded into a disposable syringe (cat. no. 302149, BD) with a Teflon needle (cat. no. FTN25G, Rokit Healthcare)

3.10 Rheological characterization of the prepared bioink

The rheological properties of the hydrogel (SA: GEL: Fg) was assessed using DHR−2 rheometer (TA instruments). Following the testing instructions, hydrogel precursor of 150 μL was firstly loaded into the gap between the parallel upper and lower plates of the rheometer (cross−hatched plate 40 mm in diameter). A temperature sweep from 37 ° C to 20 ° C, at a rate of 2° C per 120 s, was conducted on the loaded hydrogel. The influence of temperature on the rheological behavior of the storage moduli G' and loss moduli G'' were recorded at a constant frequency (1 Hz) and strain (1%). Finally, Viscosity−frequency relationship curve measured in oscillatory mode with 1% strain and 0.1−100 Hz frequency. From the measurement, the complex viscosity, $\eta* = [(G')^2 + (G'')^2]^{\frac{1}{2}}/\omega$ was calculated.

3.11 Three−dimensional bioprinting

First, a three−dimensional pattern of a mini−well chamber was designed using modeling software (CAD program Rhino 6; Robert

McNeel & Associates, Seattle, WA, USA). Then, the CAD file was converted to STL format and uploaded into the NewCreatorK V1.57.70 software (ROKIT), which was connected to a 3D printer (Invivo, Rokit; Seoul, Korea). A mini-well chamber with cross-sectional dimensions of 14 × 14 mm and 4 mm in height was printed with a thermoplastic poly(lactic acid) (PLA) polymer in a 90 mm Petri dish (one mini-well/Petri dish). Each mini-well chamber consisted of nine wells (3 × 3; individual well size: 3 mm × 3 mm). The following parameters were used to print the mini-well chamber: extruder nozzle size, 0.2 mm; layer height, 0.2 mm; printing speed, 10 mm s^{-1}; and extruder temperature, 210 ° C.

Next, a 3D construct pattern was designed using CAD software. Following the designed structure, a disposable syringe with a Teflon needle was used to deposit the bioink mixture (SA/GEL/Fg hydrogels) into a mini-well chamber. This fabrication method was used in our previous work and has proven to be effective [59]. The following parameters were used to print the hydrogel: syringe needle size, 0.2 mm; layer height, 0.2 mm; printing speed, 3 mm s^{-1}; and dispenser and bed temperature, 37 ° C. The program was run twice consecutively at the same position to generate a more stable 3D configuration with a string pattern. After 3D printing, 50 mM calcium chloride ($CaCl_2$) was added on the printed construct to crosslink SA and GEL for 10 min, and then washed twice with 1× PBS. Then, the 3D construct was further stabilized by 40U/mL thrombin (polymerized Fg) in a culture medium containing DMEM supplemented with 10% FBS for 10 min. After polymerization, the cross-linking agent was replaced with growth medium containing DMEM, 10% FBS, 50 U/mL aprotinin, 10 μg/mL EGF, and 30 μg/mL

FGF, and placed in a CO_2 incubator at 37 ° C. The medium was changed every other day.

3.12 Cell viability

Briefly, at days 0, 4, 8 and 12, a solution of DMEM containing 1 μg mL^{-1} calceim-AM and 25 μg mL^{-1} propidium iodide (PI) was used to replace the growth medium of each well containing cell-laden hydrogel and incubated at 37 ° C for 30 min. Viability of cells was estimated by counting living cells (green) and dead cells (red) on images which were randomly taken from tissue construct observed with a confocal microscope (Leica TCS SP8). Three images were taken from each tissue construct and analyzed using ImageJ. The percent of live cells among the total number of live and dead cells was used for cell viability expression.

3.13 Immunofluorescence assays

For immunofluorescence analyses, the 3D construct was fixed with 4% paraformaldehyde (PFA) for 10 min at room temperature and washed three times with PBS. The construct was incubated with phalloidin F-actin (TRITC-conjugated anti-rabbit IgG, Santa Cruz, in PBS) and or connexin 43 (FITC-conjugated anti-rabbit IgG, Santa Cruz, in PBS) for 60 min. The structure was then incubated with Hoechst stain for 10 min (nuclear staining). Finally, the samples were washed with PBS and observed using a confocal microscope (Leica TCS SP8). 3D image acquisition and analysis were performed using Las X and Imaris software.

3.14 Drug treatment and intracellular Na channel assay

The drug response to the printed construct was evaluated to verify the maturity of the fabricated cardiac construct. The printed construct was incubated with different concentrations of digoxin for

16 h and then stained with CoroNa green, a sodium-sensitive fluorescent probe.

Changes in intracellular Na^+ concentration were monitored by measuring the fluorescence emission of the cardiac 3D construct treated with the CoroNa green Na^+indicator. Stock solution of CoroNa green (cat. no. C36676) was prepared in DMSO. The stock solution was then diluted with 1× PBS to produce a 1 mM working solution. The fabricated cardiac constructs were incubated with CoroNa green solution (1 mM) for 15 min at 37 ° C. After incubation, the constructs were washed twice with 1× PBS, and 3D images were acquired using a confocal microscope.

3.15 Drug treatment and potassium channel assay

Drug-induced hERG channel blockage was tested when the cell confluence reached 80%. To screen the hERG channel blockage of small molecules (cisapride, GABA, and IMC) and the synthesized NPs (IMC-PEG-SH@Au_{19}NPs, IMC-PEG-SH@Au_{33}NPs, IMC-PEG-SH@Au_{64}NPs and F-108@TPP-AuNPs), monolayer cells and 3D cardiac constructs were treated with various concentrations of each small molecule/NP.

The permeability of the potassium channels was monitored using the FluxOR potassium channel assay kit (Invitrogen). Once inside the cardiac cell, the non-fluorescent AM ester form of the FluxOR dye is cleaved by endogenous esterases into a thallium-sensitive fluorescent indicator. After drug treatment, the monolayer cells/3D cardiac constructs were washed with 1× PBS and incubated with Tl^+ sensitive dye solution for 60 min at RT. Then, the monolayer cells/3D cardiac constructs were washed once with dye-free assay buffer before adding a final volume of assay buffer containing water-

soluble probenecid. Subsequently, the monolayer cells/3D cardiac constructs were treated with the stimulus buffer containing Tl^+ for 1 min and imaged using a confocal microscope (Leica TCS SP8). If hERG K^+ channels are not blocked, thallium ions (Tl^+) flow into the monolayer cells/cardiac construct through the K^+ channel and combine with the Tl^+-sensitive dyes to produce a fluorophore (λ_{max} 590 nm). However, when hERG K^+ channels are blocked, thallium ions (Tl^+) fail to interact with Tl^+-sensitive dyes to produce a fluorophore (λ_{max} 590 nm).

3.16 Drug treatment and hERG immunofluorescence

Changes in hERG expression were monitored by measuring the fluorescence emission of the monolayer cells/cardiac construct stained with the FITC-conjugated anti-hERG antibody. After drug treatment, the monolayer cells and 3D cardiac constructs were washed with 1× PBS. The cells were then fixed with 4% PFA for 10 min at RT and washed three times with 1× PBS. The cells were then incubated with FITC-conjugated anti-hERG antibody (Santa Cruz Biotechnology) for 60 min. Finally, the cells were washed with 1× PBS and imaged using a confocal microscope (Leica TCS SP8). 3D image acquisition and analysis were performed using Las X and Imaris software.

Results

4.1 Synthesis and characterization of IMC-PEG-SH@AuNPs

As shown in Scheme S1, the surface ligand (IMC-PEG-SH) was prepared (Sandip Gangadhar Balwe provided and co-worked the

molecule synthesis and characterization part). To investigate the effect of the surface-functionalized AuNPs on the hERG channel, a series of well-dispersed AuNPs of three different sizes (9, 17, and 46 nm) were prepared by controlling the ratio of chloroauric acid ($HAuCl_4$) to sodium citrate dihydrate ($C_6H_5Na_3O_7 \cdot 2H_2O$) (Figure 1a). The results obtained are summarized in Table S1. The three different sizes of AuNPs were functionalized with the prepared IMC-PEG-SH to form IMC-PEG-SH@AuNPs via a direct ligand exchange reaction (Scheme S2). The physicochemical characterization of the different sizes of IMC-PEG-SH@AuNPs is summarized in Table S2.

The UV-Vis spectra showed that the absorption maximum of AuNPs shifted from 521 to 529, from 524 to 542, and from 530 to 556 nm, respectively, after the introduction of the surface ligand IMC-PEG-SH (Figure 1d), indicating the successful assembly of IMC-PEG-SH@AuNP. A slight red shift in the surface plasmon resonance was observed due to the higher molecular weight of IMC-PEG-SH compared to that of citrate and the interaction of the sulfur atoms in the ligand IMC-PEG-SH with the gold surface. More red shifts were observed for larger AuNPs. As the particle diameter increased, the absorption wavelength increased and the absorption peak broadened. The hydrodynamic radii of the surface-functionalized AuNPs increased slightly, with a narrow size distribution. The measured

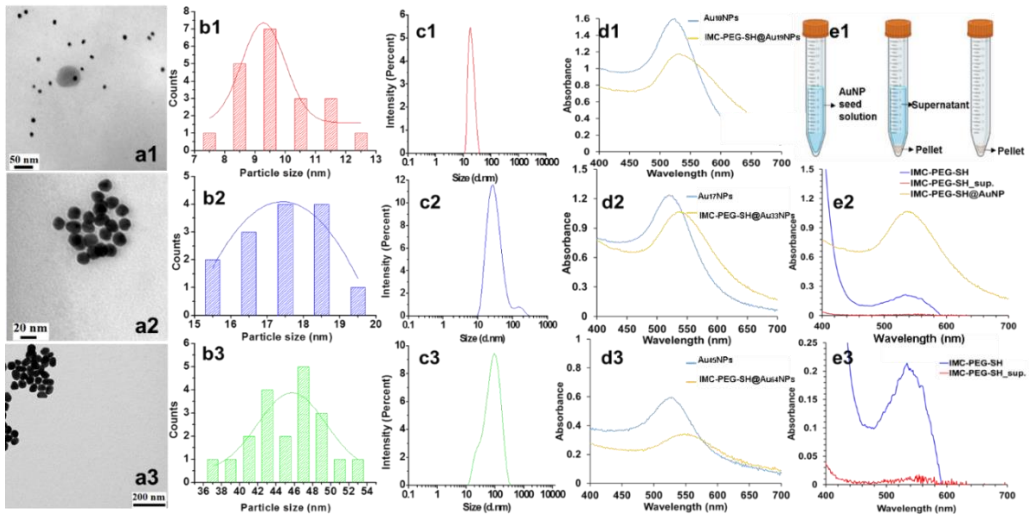

Figure 1. (a) and (b) EFTEM images and corresponding size distribution histograms of synthesized AuNPs. (a1 and b1) Au_9NPs, (a2 and b2) Au_{17}NPs, (a3 and b3) Au_{46}NPs respectively. DLS data for IMC−PEG−SH@Au_{19}NPs (c1), IMC−PEG−SH@Au_{33}NPs (c2), and IMC−PEG−SH@Au_{64}NPs (c3). (d1) UV−vis spectra of Au_9NPs (blue) and IMC−PEG−SH@Au_{19}NPs (yellow); (d2) UV−vis spectra of Au_{17}NPs (blue) and IMC−PEG−SH@Au_{33}NPs (yellow); (d3) UV−vis spectra of Au_{46}NPs (blue) and IMC−PEG−SH@Au_{64}NPs (yellow). (e1−e3) Concentration of IMC−PEG−SH bound to AuNPs. (e1) Schematic representation of the isolation of supernatant and AuNP pellet. (e2) UV−vis spectra of IMC−PEG−SH@AuNPs (yellow), IMC−PEG−SH in the supernatant after the spin down (red), and initial IMC−PEG−SH before the reaction with AuNPs (blue). (e3) is a zoom−in of spectra e2.

sizes were 19 nm, 33 nm, and 64 nm, respectively, with a polydispersity index (PDI) of less than 0.33, indicating that the particles were well dispersed (Figure 1c). After ligand exchange, the ζ−potentials of the IMC−PEG−SH@AuNPs were −19.03, −23.52, and −33.9 mV, respectively. These results show that IMC−PEG−SH@AuNPs have a slightly lower ζ−potential than the

corresponding citrate-capped AuNPs because the surface ligand IMC-PEG-SH is not negatively charged. The obtained results were summarized in Table S2.

4.2 Synthesis and characterization of F-108@TPP-AuNPs

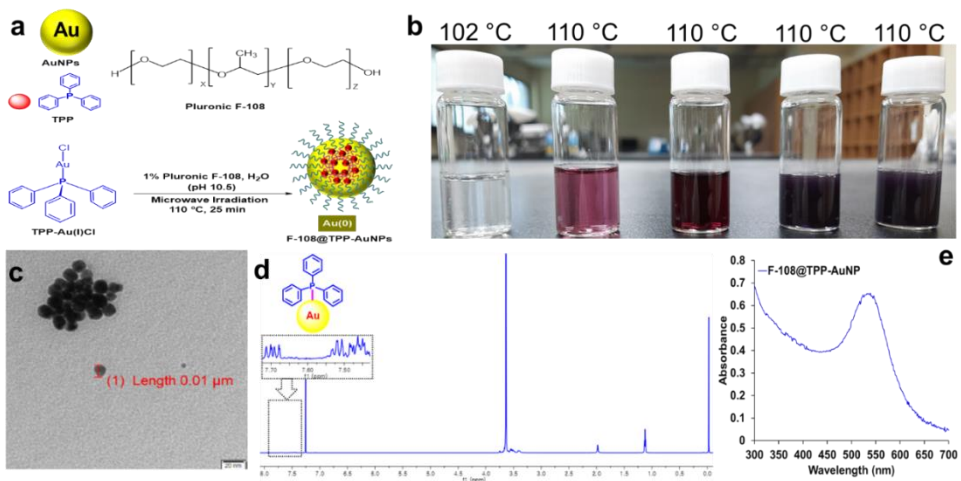

Figure 2. (a) Schematic representation of the synthesis of F-108@TPP-AuNPs. (b) Color changes in F-108@TPP-AuNPs observed by the optimization of reaction conditions for the synthesis of F-108@TPP-AuNPs. (c) EFTEM image of F-108@TPP-AuNPs. (d) ^{1}H NMR spectra of F-108@TPP-AuNPs in $CDCl_3$. (e) Absorption spectrum of F-108@TPP-AuNPs in H_2O.

Figure 2b shows the F-108@TPP-AuNPs obtained as a function of the temperature and reaction time (Sandip Gangadhar Balwe provided and co-worked the molecule synthesis and characterization part. The reaction was monitored by the color change in the solution, from colorless to red, indicating the formation of F-108@TPP-AuNPs. Initially, the reaction was carried out at 102 ° C for 20 min under microwave irradiation. However, no color change was observed. The

reaction temperature was then increased to 110 ° C, and the solution was irradiated for 20 min. Notably, a light pink color was observed. Then, the reactions were carried out at same temperature of 110 ° C with increasing reaction times of 25, 30, and 60 min. At a reaction time of 25 min, the formation of red F-108@TPP-AuNP occurred. The reaction conditions of 110 ° C and 25 min provided the most stable F-108@TPP-AuNPs. The absorption spectrum of F-108@TPP-AuNPs (Figure 2e) exhibits a narrow single peak centered at 532 nm, assigned to the surface plasmon resonance of F-108@TPP-AuNPs, representing the formation of F-108@TPP-AuNPs. The size and shape of F-108@TPP-AuNPs were confirmed using EFTEM (Figure 2c). The F-108@TPP-AuNPs were spherical in shape, with an average size of ~10 nm. ^{1}H NMR spectroscopy was used to investigate the chemical composition of the F-108@TPP-AuNP surface (Figure 2d). In the aromatic region, proton peaks from the phenyl rings of triphenylphosphinegold(I)chloride ($(Ph_3P)AuCl$) appeared as a multiplet in the region of 7.44-7.56 ppm, while conjugated on the surface of AuNPs, three distinct multiplets were observed in the region of 7.43-7.72 ppm, which resulted from differential shielding of the protons in the ortho, meta, and para positions of the ligand upon binding to the metal atoms on the surface of the gold nanoparticles. Furthermore, a set of peaks corresponding to the F-108 pluronic polymer protons was also present as a triplet at 1.13 and a singlet at 3.64 ppm. ^{1}H NMR spectroscopic data clearly confirmed the presence of both the F-108 pluronic polymer and TPP molecules on the surface of the AuNPs.

4.3 Concentration of IMC−PEG−SH bound to AuNPs

After the reaction, the conjugate IMC−PEG−SH@AuNPs were centrifuged and the supernatant containing IMC−PEG−SH unbound to AuNPs was collected (Figure 1 e1).

The concentration of unbound surface ligand was determined using the following equation:

$$C_{ligand,unbound} = \left[\frac{\left(C_{ligand,alone} \ X \ A_{ligand,unbound}\right)}{A_{ligand,alone}}\right]$$

where $C_{ligand,unbound}$ is the concentration of unbound IMC−PEG−SH in the supernatant, $C_{ligand,alone}$ is the concentration of IMC−PEG−SH alone, $A_{ligand,alone}$ is the absorbance of IMC−PEG−SH alone, and $A_{ligand,unbound}$ is the absorbance of unbound IMC−PEG−SH. The concentration of the ligand conjugated to the surface of the AuNPs was determined using the following equation:

$$C_{ligand,NP} = C_{ligand,initial} - C_{ligand,unbound}$$

where $C_{ligand,NP}$ is the concentration of IMC−PEG−SH ligand conjugated to the surface of AuNPs, $C_{ligand,initial}$ (10 mM) is the initial concentration of IMC−PEG−SH ligand used to react with AuNPs, and $C_{ligand,unbound}$ is the concentration of unbound IMC−PEG−SH present in the supernatant. Based on the above equation, the concentrations of IMC−PEG−SH ligand conjugated on the surfaces of Au_9NPs, Au_{17}NPs, and Au_{46}NPs were determined to be 9.50 mM, 9.56 mM, and 9.14 mM, respectively. Based on this determination, stock solutions of IMC−PEG−SH@Au_{19}NPs, IMC−PEG−SH@Au_{33}NPs, and IMC−PEG−SH@Au_{64}NPs were prepared such that their working concentration range was set to be the same to compare their hERG channel blockage as a function of nanomaterial size.

4.4 Designing patterns for 3D bioprinting

The SFP model uses a computer-aided design file (CAD) to design and print the cardiac tissue construct. The CAD files were then converted to g-code, which transmitted the desired print pattern and parameters to the 3D printer. Figure 3a and 3b shows the CAD design and the 3D printed image of the construct, respectively. The printing conditions were as follows: The syringe needle size was 0.2 mm, the layer height was 0.2 mm, and the printing speed was 3 mm s^{-1}. These printing conditions were used in our previous work and proved to be effective [59].

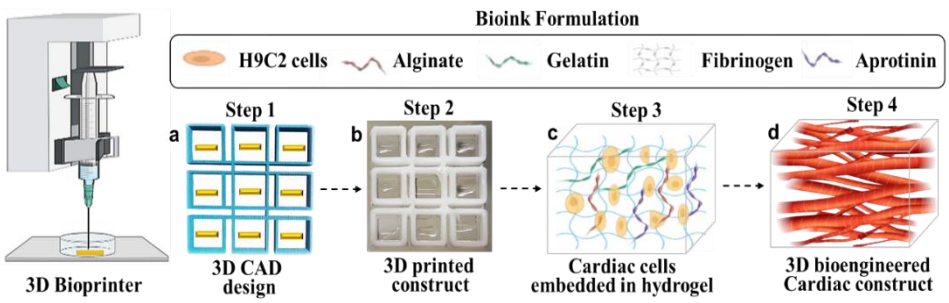

Figure 3. (a and b) Represents the CAD design and the 3D printed image of the construct, respectively. (c) Schematic diagram of the printed construct showing homogenous mixture of cardiac cells embedded in hydrogel. (d) Schematic diagram showing the branched and multinucleated cardiac tissue cells, which is applied for in situ detection of drug-induced sodium and potassium ion channel responses.

4.5 Biomaterials for cardiac tissue engineering

The biomaterials used in this study for cardiac tissue engineering are sodium alginate (SA), gelatin (GEL), fibrinogen (Fg), and aprotinin (APRO). These four components of bioink have different roles in the bioprinting and tissue generation process: SA serves as a temporary material template that allows controlled deposition of the hydrogel by

the extruder; GEL supports cell adhesion and proliferation and also allows modification of the viscosity of the hydrogel to meet extrusion and printing criteria; and Fg provides a tailored matrix (stabilized by thrombin cross-linking) for cell spreading and differentiation during long in vitro cultures. APRO is a protease inhibitor that can stop or slow down fibrin degradation (thrombin converts Fg to fibrin) within a few days. Therefore, to ensure proper tissue development, fibrin degradation was controlled by adding aprotinin to both the bioink formulation and the tissue culture medium.

4.6 Rheological study

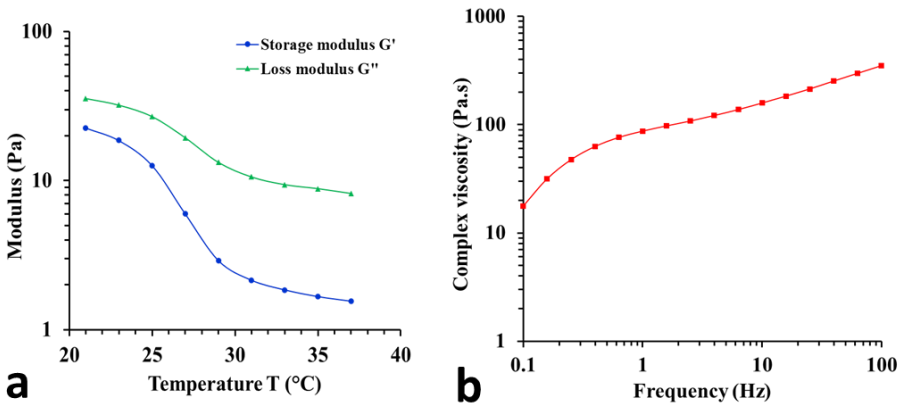

Figure 4. (a and b) Rheological properties of the bioink: (a) Temperature-controlled rheological behavior of the hydrogel showing the storage modulus (G′) and loss modulus ((G″) as a function of temperature at a constant 1% strain and 1 Hz frequency. (b) Viscosity-frequency relationship curve measured in oscillatory mode with 1% strain and 0.1-100 Hz frequency.

Rheological characterization was performed to investigate the viscosity and storage modulus of the bioink (SA:GEL:Fg hydrogel mixture). The variation of storage modulus (G') and loss modulus (G")

of the bioink was recorded with the change of temperature (from 20 to 40 ° C at a rate of 2 ° C min^{-1}). As shown in Figure 4a, the storage modulus was lower than the loss modulus (G'< G"), mainly indicating the viscous properties and liquid-like behavior of the hydrogel and demonstrating the single-stranded arrangement of the components of the bioink. A sharp increase in G' and G" was observed as the temperature decreased, indicating gel formation. Upon heating, the hydrogel showed thermos reversible behavior, and the values of G' and G" decreased. From these temperature sweep results, it is clear that the hydrogel in the developed SFP-based system exhibits liquid-like behavior and that a crosslinking process is essential to stabilize the printed structures.

Figure 4b shows the measurements of viscosity, $\eta*$, over a frequency sweep. A linear increase in the viscosity profile as a function of frequency was observed. This linear viscoelastic regime shows that the hydrogel behaves as a viscous material over a wide range of frequencies (G"> G'). At low frequencies, the material behavior becomes liquid-like, which is important for gel composition. This is because the liquid-like behavior of the hydrogel helps the gel to pass through the needle. Therefore, the bioink was precisely applied to assemble a high-resolution scaffold-free de novo model. To further stabilize the printed structures, the samples were subjected to a double crosslinking step (solution with 50mM $CaCl_2$ and 40U/mL thrombin: $CaCl_2$ for SA and GEL and thrombin for Fg) in which SA, GEL and Fg were polymerized for 20 minutes to form a covalently crosslinked network. After crosslinking, the storage modulus G' of the crosslinked hydrogel becomes larger than the loss modulus G''. This increase in storage modulus is sufficient for the gel

to keep the cells intact and still allow them to proliferate in the bioprinted hydrogel. These observations have been previously verified and reported [60,61].

4.7 Generation of biomimetic cardiac cell structure

As shown in Figure 5a, shortly after their encapsulation in the hydrogels, the cardiac cells appeared as single cells homogeneously distributed throughout the volume of the samples. However, as the cultivation period progressed, the individual cardiac cells began to elongate (Figure 5a – day 4, day 8 and day 12). This is a common

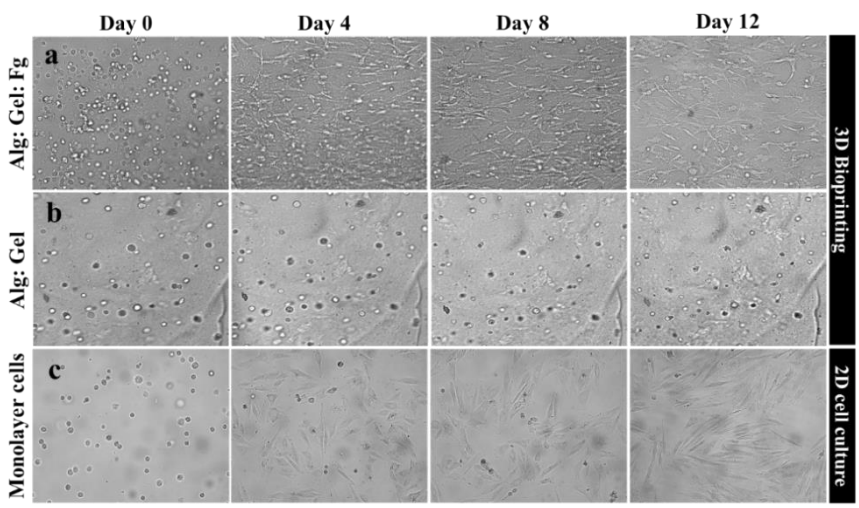

Figure 5. (a) 3D bioprinting of cardiac cell–laden hydrogel containing sodium alginate, gelatin and fibrinogen. (b) 3D bioprinting of cardiac cell–laden hydrogel containing sodium alginate and gelatin alone (without fibrinogen) and (c) 2D cell image: H9C2 cells grown in flat–bottom surface.

feature of proliferating cardiac cells. The most pronounced histological feature of the bioprinted cardiac tissue was the formation of dense and uniformly aligned cardiac muscle bundles. To illustrate the importance of the biomaterial components, two different bioink (1. bioink with fibrinogen and 2. bioink without fibrinogen) were

prepared and used to print the cardiac cells. In in vitro culture, the construct (cells printed without Fg) was dominated by circular cells after 12 days in culture (Figure 5b). However, the number of elongated cells in the construct (with Fg printed cells) increased after 12 days in culture (Figure5a). Finally, the bioprinted cardiac constructs (cells printed with Fg) developed as aligned cardiomyocytes with a clear sarcomere structure that filled the entire space of the construct within two weeks in culture. This effect is easily explained by the presence of Fg, and diffusion of oxygen and nutrients within the hydrogel is possible in the largest internal volume. In contrast, the bioprinted sample without Fg showed no cell growth or heterogeneity, confirming the role of Fg in recapitulating the cardiac structure.

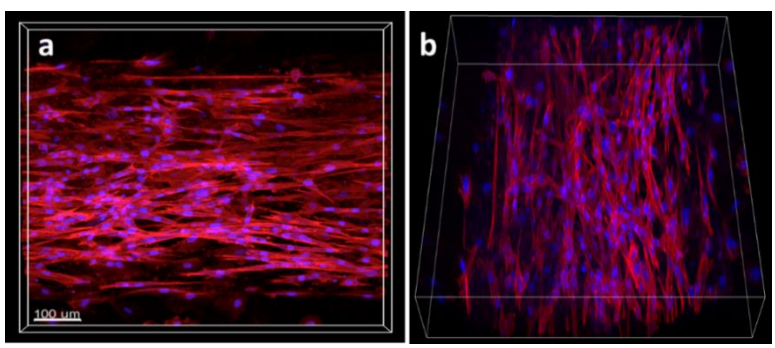

Figure 6. (a) Top view and (b) Cross view of 3D cardiac tissue construct image stained with fluorescent labelled phalloidin and Hoechst.

In 2D cell culture, cell morphology differs from native tissue due to the additional surface tension and unilateral cell adhesion in the cell culture flask or dish (Figure5c). In addition, monolayer cell culture cannot adequately explain the clinically relevant models of heart disease. Therefore, various 3D printing techniques and designs have been applied to manipulate cell physiology through selective choice of substrate, topography, and material stimulation by electrical or

mechanical signals. Figure 6a (top view) and 6b (transverse view) show the fluorescence images of bioprinted cardiac cells stained with phalloidin F-actin and Hoechst, respectively, showing the 3D morphology of the cardiac cells in the bioprinted construct. Compared with the 2D cell culture (Figure 7a and 7b: monolayer cells grown in flat-bottom cell culture plate), the 3D bioprinted cardiac cells (Figure 7c and 7d: cells embedded in bioink and printed in flat-bottom cell culture plate) eventually began to elongate within the bioprinted construct. Aligned cardiomyocytes with clear sarcomeres were generated using an SFP-based bioprinting technique (Figure 8). Aligned cardiomyocytes with a clear sarcomere structure are a common feature of proliferating cardiac cells.

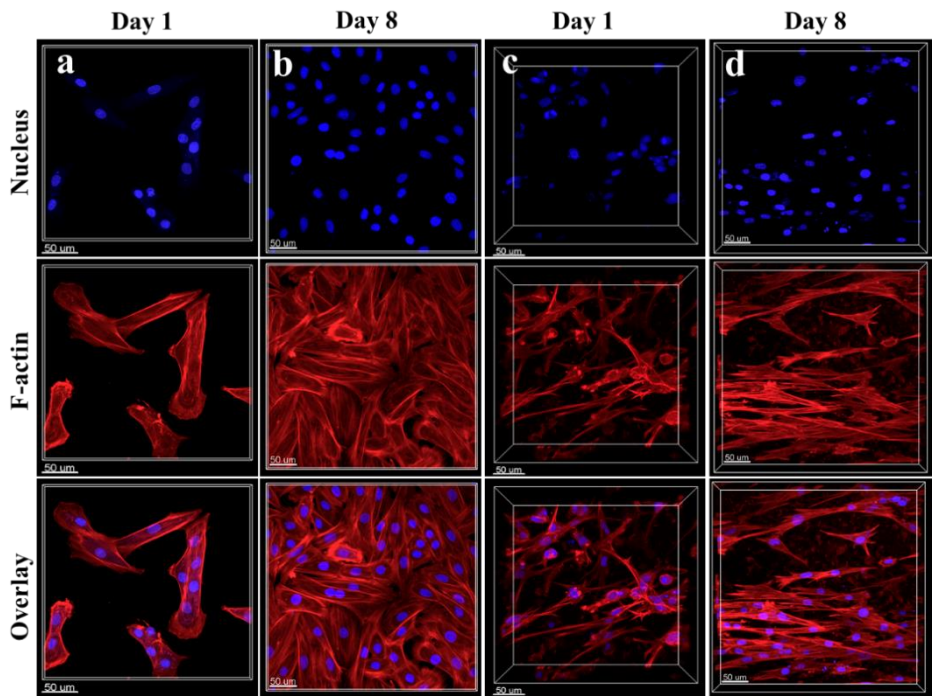

Figure 7. Immunofluorescent staining (fluorescent labelled phalloidin and Hoechst) of H9C2 cells grown in flat-bottom surface (a - Day 1, b - Day 8) and 3D bioprinted hydrogel (c - Day 1, d - Day 8).

4.8 Cell viability of the printed cardiac cells

The printed cardiac cells were incubated in vitro for at least two weeks, and their viability was assessed by quantification of live and dead cells on the SFP-based hydrogel matrix. As shown in Figure 9a, the printed cells in the construct showed no serious changes in cellular viability from day 0 to day 12, indicating the biocompatibility of the hydrogel used in this study.

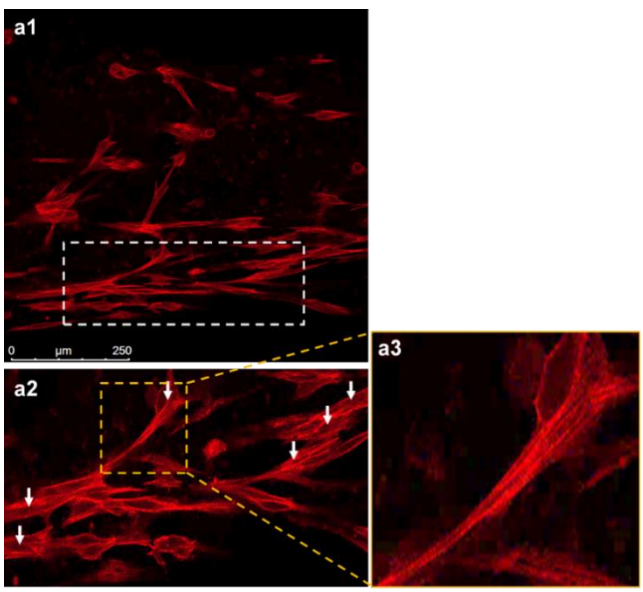

Figure 8. (a1) A single plane image at Z = 20 μm from figure 13e. (a2) Magnified image of white boxed area in image a1. Aligned cardiomyocytes with sarcomeres are indicated with arrow mark. The arrow indicates, the filling inside thick cellular cytoplasm is called z line pattern, which confirms sarcomere. (a3) Magnified image of white boxed area in image a2. Aligned F-actin-based thin filaments within sarcomeres were represented.

In Figure 9b, the primary Y axis shows a high viability of the printed cells at day 0 and a slight decrease in the viability of the cells at day 12 within the printed construct. The secondary Y-axis shows an increase in cell number over the culture period due to cell

proliferation. These results prove that the cell printing process followed by double crosslinking is gentle and ensures high cell viability after printing.

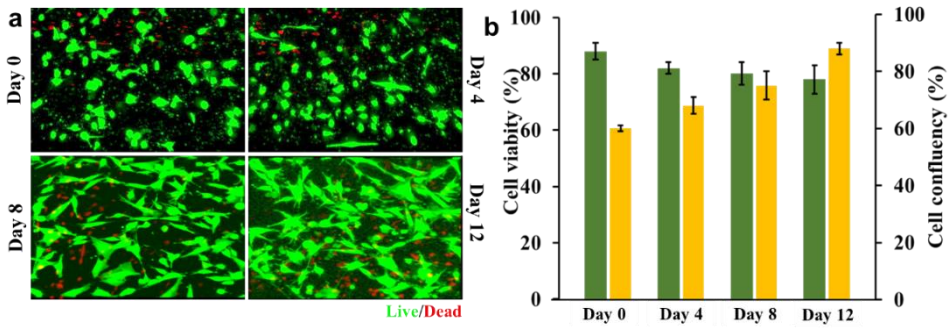

Figure 9. Cell viability and confluency was assayed by Live/Dead cell staining on cell-laden hydrogel. (a) Representative live/dead images of H9C2 cells grown on SFP-based hydrogel matrix, (b) their viability and confluency on day 0, 4, 8 and 12 of in vitro culture. Error bars represent the standard deviation of three independent measurements.

4.9 Immunofluorescence Staining and Imaging for the Assessment of 3D bioprinted cardiomyocytes

The 3D cardiac tissue prepared with SFP achieved high confluence with the formation of tight intracellular junctions. At a specific time point (12 days), a qualitative assay (immunofluorescence) was performed to evaluate the differentiation state of the 3D cardiac tissue prepared with SFP. Confocal microscopy revealed the presence of connexin 43 (Cx43), a gap junction protein that enables electrical coupling between cardiomyocytes, localized at cell-cell boundaries. Compared with 2D cell cultures (Figure 11), expression of Cx43 was markedly increased in 3D bioprinted cardiac cells (Figure 10a). Single plane images clearly showed expression of Cx43 in the printed construct (Figure 10b-10d). A side view of the 3D

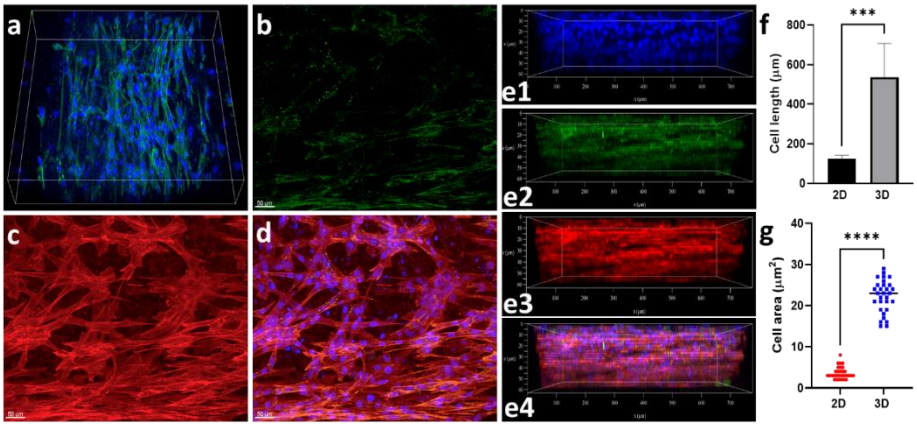

Figure 10. (a) 3D cardiac tissue construct image stained with fluorescent labelled anti-connexin 43 (Cx43) antibody and Hoechst. b-d (A single plane image at Z = 30 μm) represent images corresponding to (a): Cx43 alone (b), F-actin alone (c), and merge of all channel (d). (e1-e4) Side view image of 3D cardiac tissue imaged through a depth of 70 μm. (e1) Hoechst alone, (e2) Cx43 alone, (e3) F-actin alone, and (e4) merge of all channel. (a-e): 20× objective, stacking size: 70 μm, step size: 3 μm. Three-dimensional images were acquired using a Leica TCS SP8 DMI8-CS system equipped with the 20×/0.75 IMM objective and data were analyzed using Imaris software. 2D vs 3D cardiac cell dimension; cell length (f), and cell area (g), presented as mean values ±SD. Error bars represent the standard deviation of three independent measurements.*Indicates $p < 0.05$.

image showed the distribution of F-actin, Cx43, and the nucleus in the bioprinted construct (Figure 10 e1-e4). Thus, overexpression of Cx43 in 3D-printed cardiac cells might be related to better and more functional organization of the 3D-bioprinted cardiac construct. Figure 10f and 10g show the quantitative assessment of cell growth under 2D and 3D growth conditions in terms of cell length and covered cell area during 12 days of cultivation. A rapid increase in cell area, length, and orientation of 3D bioprinted cardiomyocytes

compared with 2D cell culture was observed. Overall, the bioprinted cardiac tissue developed from single, separate cardiomyocytes to a contiguous, aligned, and densely stained cardiac tissue that filled the entire construct. Thus, the proposed de novo–based regeneration of cardiac tissue represents a major milestone and confirms that the 3D bioprinted model is an excellent approach to mimic the structure and functionality of cardiac tissue in vitro.

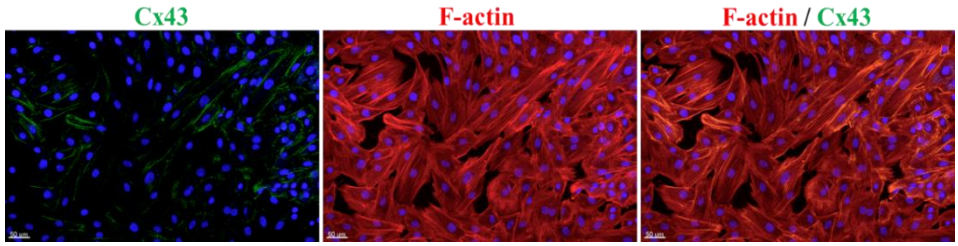

Figure 11. Immunofluorescent staining (fluorescent labelled Cx43 antibody, phalloidin and Hoechst) of H9C2 cells grown in flat–bottom surface.

4.10 In situ measurements of small–molecule–induced sodium ion channel responses using 3D biomimetic cardiac constructs

To evaluate the functionality of the regenerated cardiac construct, the common cardiac drug digoxin was used. Digoxin is a cardiac glycoside used to treat atrial fibrillation and/or heart failure. It inhibits Na^+/K^+ ATPase in cardiac myocytes, resulting in an increase in intracellular sodium concentration. To test our SFP cardiac construct, we dosed our samples with 250 nM and 500 nM digoxin. The effect of the drug on intracellular Na^+ levels was monitored using the Na^+ indicator. Drug–treated and untreated cardiac constructs were subjected to the CoroNa™ green assay. Figure 12a–12c (3D image – top view) shows the effect of digoxin on intracellular Na^+ level. In the control group (Figure 12a: untreated heart construct), a

lower number of Na^+ indicator-positive fluorescent cells were observed, whereas the number of Na^+ indicator-positive fluorescent cells increased significantly with the increase in digoxin concentration (Figure 12b and 12c).

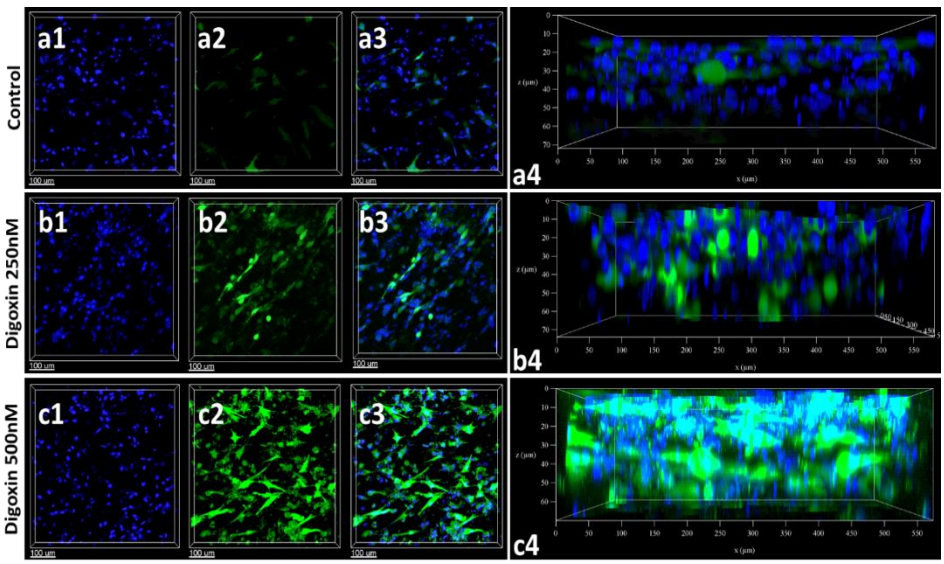

Figure 12. *In situ* detection of sodium channel response to cardiac drug, digoxin (images acquired in region I). Top view of 3D cardiac tissue image: (a1-c1) Hoechst alone, (a2-c2) sodium ion images, and (a3-c3) merge of all channel. (a4-c4) Bottom view image of 3D cardiac tissue imaged through a depth of 70 μm. (a-c): 20× objective, stacking size: 70 μm, step size: 3 μm. Three-dimensional images were acquired using a Leica TCS SP8 DMI8-CS system equipped with the 20×/0.75 IMM objective.

Figure 12a4-c4 (3D image-bottom view) clearly shows that cardiac constructs treated with digoxin had a greater number of Na^+-positive cells than the control group. This trend was significant and consistent across the different regions of the bioprinted construct. These results confirm that digoxin-induced inhibition of the Na^+ pump leads to increased Na^+ levels by decreasing the rate of Na^+ influx through the Na^+/Ca^{2+} exchanger. Therefore, the developed system can

accurately assess the response of the cardiac construct to the drug by measuring the fluorescence signal generated in the 3D cardiac construct.

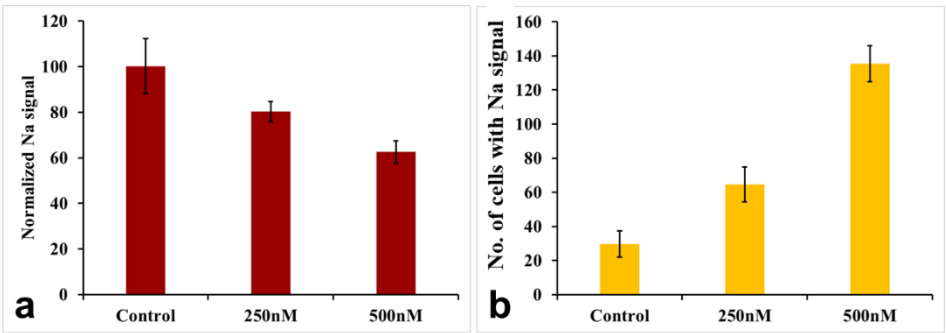

Figure 13. (a and b) Represents normalized Na signal and number of cells with sodium signal in the cardiac construct, respectively. Error bars represent the standard deviation of three independent measurements.

4.11 In situ measurements of small-molecule-induced hERG potassium ion channel blockage using 3D biomimetic cardiac constructs

Three different small molecules, cisapride, gamma-aminobutyric acid (GABA), and indomethacin (IMC), were used to investigate the potential impact of small molecules on the hERG potassium channel. When the cells were treated with cisapride and IMC, they were bound to the drug binding sites in the hERG channel and blocked the channel activity, as observed through a reduction in hERG immunofluorescence. However, when the cells were treated with GABA, hERG channel activity was not blocked, and hERG immunofluorescence remained unaffected. Similarly, when the cells were exposed to cisapride and IMC, the K^+ channels were blocked, and thallium ions (Tl^+) failed to interact with the Tl^+-sensitive dyes to produce a fluorophore (Figure 14a; right panel). However, when

the cells were treated with GABA, the K^+ channels were not blocked. Therefore, Tl^+ flows through open hERG K^+ channels and combines with Tl^+-sensitive dyes to produce a fluorophore (Figure 14b; left panel). An increase in drug concentration led to a decrease in the permeability of K^+. Hence, a lower number of K^+-indicator positive fluorescent cells was observed in the cisapride-treated and IMC-treated sets (Figure 14c and 14g: treated cardiac construct; left panel), compared with the control without drug treatment (Figure 14c and 14g: untreated cardiac construct; left panel). These results indicate that the permeability of the K^+ channel was blocked in proportion to an increase in the treatment dose over the tested drug concentration range.

Similarly, a significant reduction in hERG immunofluorescence was observed in the cisapride-treated and IMC-treated groups (Figure 14c and 14g: treated cardiac construct; right panel), whereas hERG immunofluorescence was unaffected in the control group (Figure 14c and 14g: untreated cardiac construct; right panel). In contrast, GABA did not show any significant effect on the K^+ channel blockage over the tested concentration range (1, 10, and 20 μM) (Figure 14f). The permeability of the K^+ channel (Figure 14e:3D image - top view; left panel) and hERG immunofluorescence (Figure 14e:3D image - top view; right panel) in the treated cells remained almost the same as those in the control over the entire drug range tested. Thus, intracellular homeostasis was well-conserved in the GABA-treated cardiac construct.

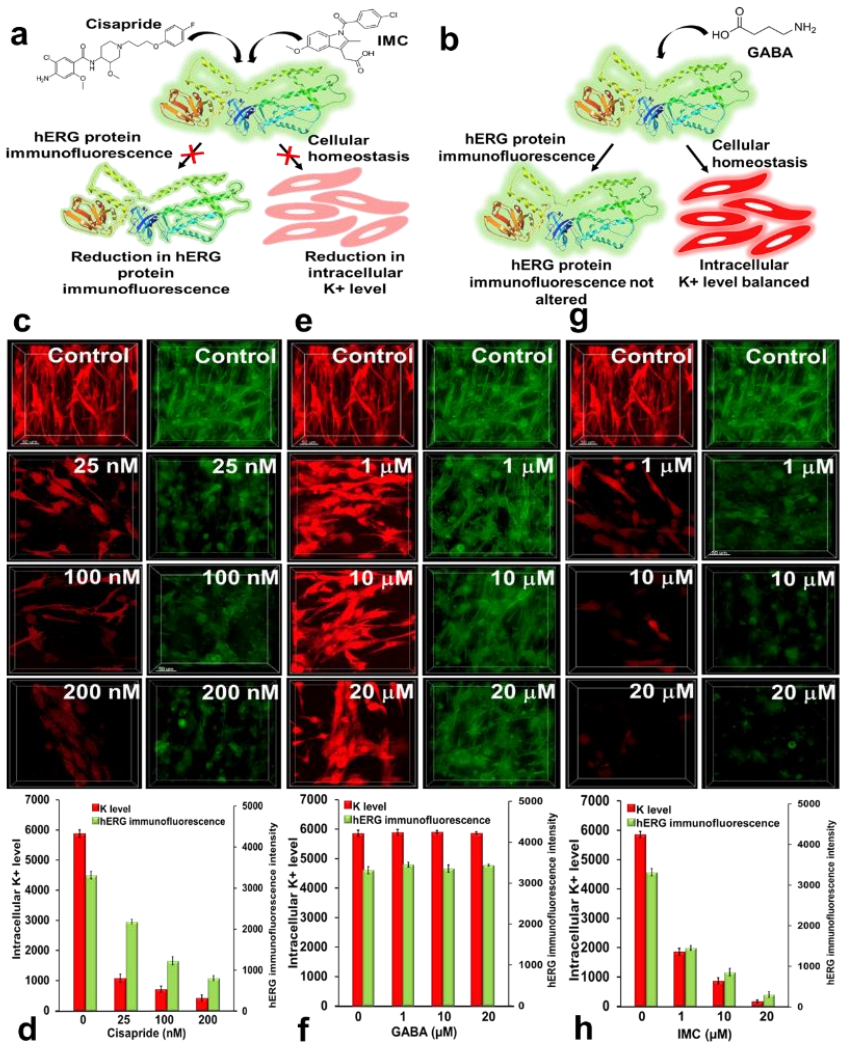

Figure 14. (a and b) Schematic illustration of small molecule–induced hERG potassium blockage. (c), (e), and (g) represents the permeability of the K+ channel (3D image – top view; left panel) and intracellular hERG immunofluorescence (3D image – top view; right panel) in 3D bioengineered cardiac constructs, obtained with various concentrations of cisapride (25nM, 100nM, and 200nM), GABA (1μM, 10μM, and 20μM), and IMC (1μM, 10μM, and 20μM), respectively. (d), (f), and (h) represent average fluorescence signals of the K+ indicator and hERG immunofluorescence in 3D bioengineered cardiac constructs, obtained with

various concentrations of cisapride, GABA, and IMC, respectively. Error bars represent the standard deviation of three independent measurements.

4.12 In situ measurements of F-108@TPP-AuNP-induced hERG potassium ion channel blockage using 3D biomimetic cardiac constructs

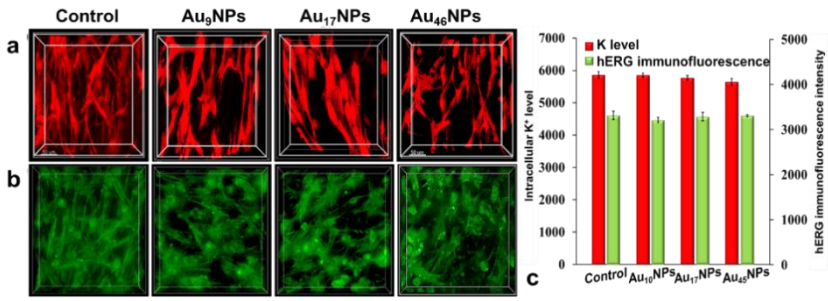

Figure 15. (a) and (b) represents the permeability of the K^+ channel (3D image – top view; top panel) and intracellular hERG immunofluorescence (3D image – top view; bottom panel) in 3D bioengineered cardiac constructs, obtained with 5μM of AuNPs. (c) represent average fluorescence signals of the K^+ indicator and hERG immunofluorescence in 3D bioengineered cardiac constructs, obtained with various concentrations of AuNPs. Error bars represent the standard deviation of three independent measurements.

As shown in Figure 15, AuNPs (Au_9NPs, Au_{17}NPs, and Au_{46}NPs) did not show any significant effect on the hERG K^+ channel blockage over the tested concentration range. The permeability of the K^+ channels and hERG protein immunofluorescence in the treated cells remained almost the same as that in the control. These results clearly suggest that intracellular homeostasis is well conserved in AuNP-treated cardiac constructs. To test the influence of AuNPs and their surface functionalization, an NP termed F-108@TPP-AuNP was newly synthesized and tested to determine its effect on the permeability of

K^+ channels and hERG immunofluorescence. When the cells were treated with F-108@TPP-AuNPs, the cardiac constructs emitting fluorescence showed a dose-dependent difference in the permeability of K^+ and hERG protein blocks. A significant decrease in the permeability of K^+ ions was observed as the concentration of F-108@TPP-AuNPs increased.

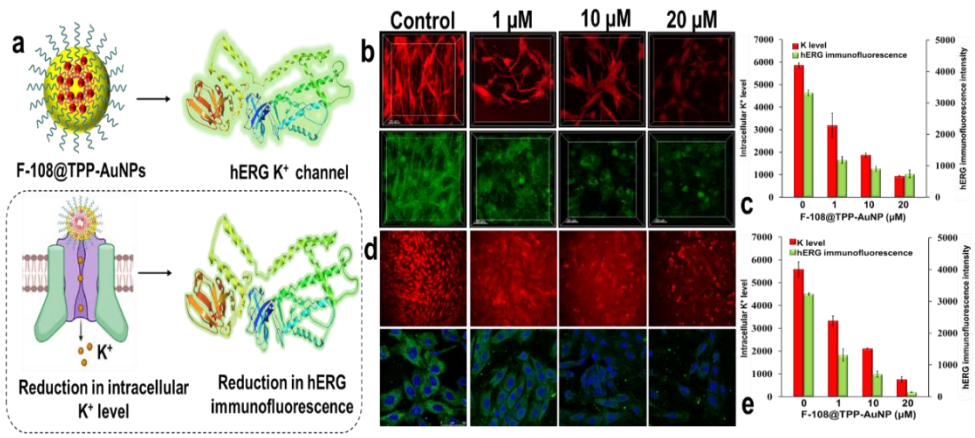

Figure 16. (a) Schematic illustration of F-108@TPP-AuNP-induced hERG potassium blockage. (b) represents permeability of the K^+ channel (3D image - top view; top panel) and intracellular hERG immunofluorescence (3D image - top view; bottom panel) in 3D bioengineered cardiac constructs, obtained with various concentrations of F-108@TPP-AuNPs (1μM, 10μM, and 20μM). (c) represents average fluorescence signals of the K^+ indicator and hERG immunofluorescence in 3D bioengineered cardiac constructs. (d) represents permeability of the K^+ channel (2D image; top panel) and intracellular hERG immunofluorescence (2D image; bottom panel) in monolayer cells treated with various concentrations of F-108@TPP-AuNPs (1μM, 10μM, and 20μM). (e) average fluorescence signals of the K^+ indicator and hERG immunofluorescence in monolayer cells treated with various concentrations of F-108@TPP-AuNPs, respectively. Error bars represent the standard deviation of three independent measurements.

3D-top view images showed a lower number of K^+-indicator positive fluorescent cells in the F-108@TPP-AuNPs-treated cardiac constructs than in the control. These results indicate that the permeability of the K^+ channel was blocked in proportion to an increase in the treatment dose over the tested NP concentration range. A similar tendency was observed for the reduction of hERG protein immunofluorescence. The reduction in permeability of the K^+ channel/hERG protein immunofluorescence in the cardiac constructs induced by F-108@TPP-AuNPs was quantitatively plotted as a function of the concentration of F-108@TPP-AuNPs (Figure 16c and 16e).

4.13 Verification of size-dependent effect of the nanomaterials on the hERG potassium ion channel blockage using 3D biomimetic cardiac constructs

To further investigate the influence of nanomaterial size and AuNP ligands on hERG channel blockage, three different sizes of IMC-PEG-SH@AuNPs (~19 nm, ~33 nm, and ~64 nm) were used for the quantitative evaluation using 3D bioengineered cardiac constructs. The dose-dependent reduction in the permeability of the K^+ channel and hERG protein immunofluorescence caused by IMC-PEG-SH@AuNPs was quantitatively plotted to clearly reveal and compare such effects among the different sizes of IMC-PEG-SH@AuNPs (Figures 17b, 17d, and 17f). The degree of reduction in the permeability of the K^+ channel and hERG protein immunofluorescence increased as the size of the IMC-PEG-SH@AuNPs increased, under the condition of identical concentrations of IMC-PEG-SH ligand bound on the surface of

AuNPs. NP size-dependent inhibition of K^+ permeability decreases K^+ levels by diminishing the rate of K^+ influx through the Na^+/K^+ exchanger, thereby ultimately reducing hERG immunofluorescence and impairing cellular homeostasis.

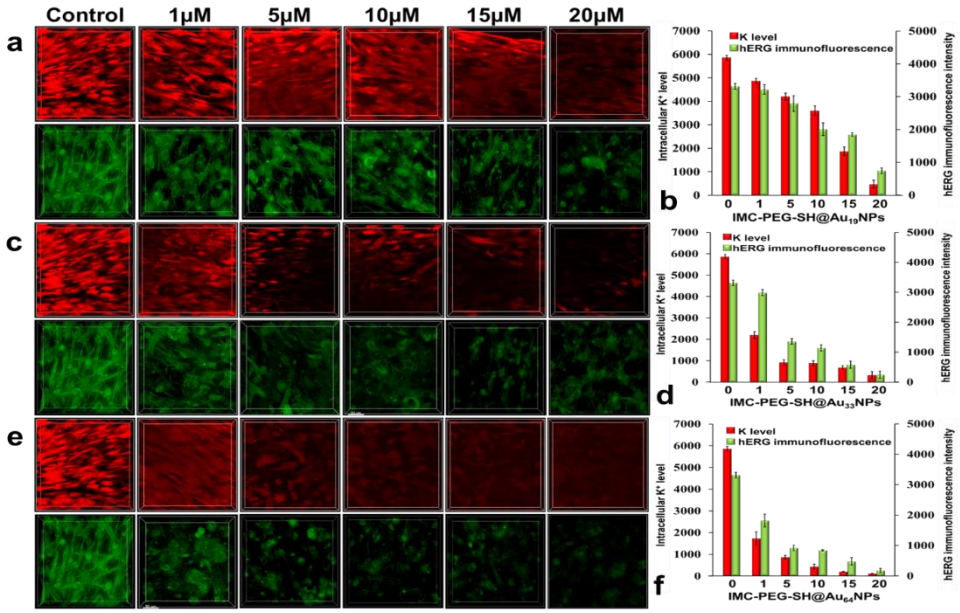

Figure 17. (a), (c), and (e) represent permeability of the K^+ channel (3D image – top view; top panel) and intracellular hERG immunofluorescence (3D image – top view; bottom panel) in 3D bioengineered cardiac constructs, obtained with various concentrations (1μM, 5 μM, 10μM, 15μM, and 20μM) of IMC-PEG-SH@Au_{19}NPs, IMC-PEG-SH@Au_{33}NPs, and IMC-PEG-SH@Au_{64}NPs, respectively. (b), (d), and (f) represent average fluorescence signals of the K^+ indicator and hERG immunofluorescence in 3D bioengineered cardiac constructs, obtained with various concentrations (1μM, 5 μM, 10μM, 15μM, and 20μM) of IMC-PEG-SH@Au_{19}NPs, IMC-PEG-SH@Au_{33}NPs, and IMC-PEG-SH@Au_{64}NPs, respectively. Error bars represent the standard deviation of three independent measurements.

4.14 Molecular docking study

From the protein (hERG)-ligand (IMC-PEG-SH) interaction, it can be observed that the aromatic amino acid residue Phe-656 has a

strong $\pi-\pi$ stacked interaction with the indole moiety of IMC-PEG-SH at a distance of 4.26 Å. The pore helix amino acid residue Thr-623, present in the domain of the hERG protein, forms a strong $\pi-\sigma$ interaction with the phenyl ring of IMC-PEG-SH at a distance of 3.66 Å. In addition, the amino acid residue Ser-624 forms a carbon hydrogen bond with a distance of 2.72 Å. These results indicate the main reason for the stability of IMC-PEG-SH within the binding pocket of the target protein hERG.

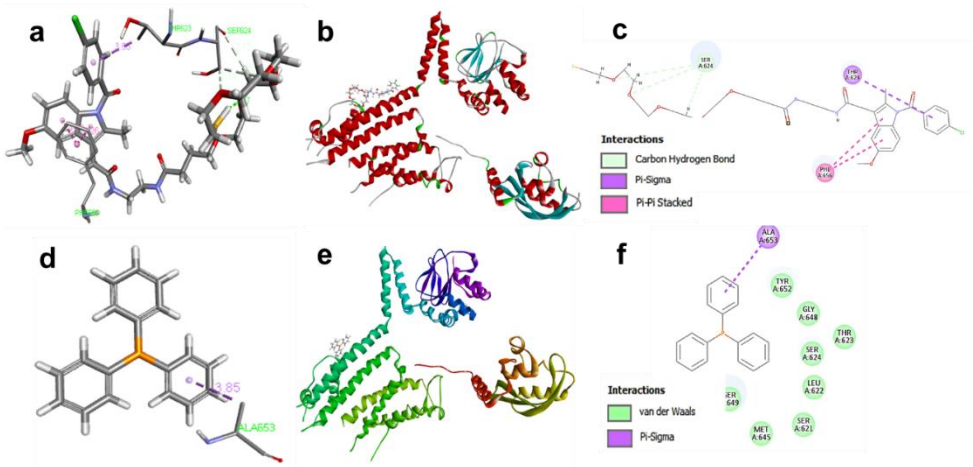

Figure 18. (a) and (b) represent molecular docking of IMC-PEG-SH with hERG protein (3D image). (c) Two-dimensional image of amino acid residues involved in interactions between hERG protein and IMC-PEG-SH. (d) and (e) represent molecular docking of TPP with hERG protein (3D image). (f) Two-dimensional image of amino acid residues involved in interactions between hERG protein and TPP.

From the protein (hERG)-ligand (TPP) interaction, it can be clearly observed that the amino acid residues Tyr-652, Thr-623, and Ser-624 have a van der Waals interaction with the phenyl ring of TPP. Moreover, the amino acid residue Ala-653 present in the hERG protein domain forms a $\pi-\sigma$ interaction with the phenyl ring of TPP

at a distance of 3.85 Å. This may be the reason for the stability of TPP within the binding pocket of the target protein hERG.

Discussion

2D cell-based screening assays are commonly performed to evaluate new early-stage drug candidates. Although 2D in vitro cell models offer high throughput, they often provide incorrect predictions because of the oversimplified microenvironment of the cells [37-39]. Over the past decade, many studies have shown that 3D in vitro tissue models can better mimic the natural microarchitecture and physiological functions of the heart than 2D models [62-64]. In addition, downsizing tissue models to microtissues can reduce the consumption of cells and other components while maintaining the functionality of the tissue. The overall goal of this study was to implement and propose 3D biomimetic cardiac constructs as a platform for drug screening to investigate the responses of sodium and hERG potassium channels to drugs.

First, we developed a scaffold-free 3D-printed model. In this work, we encapsulated the cells in an ECM with sodium alginate, gelatin, and fibrinogen to produce biomimetic 3D cardiac tissue models. This allows the cardiac cells to float in 3D space as they expand and form connections. The SFP system helps create a 3D hydrogel construct that encapsulates biological cells. As a result of the rapid printing, the cells spend little time out of culture, so the printed cardiac cells maintain high cell viability and appropriate cell activities. We have successfully printed cardiac cells and produced a 3D biomimetic cardiac construct using the SFP system.

Four different small molecules (digoxin, cisapride, gamma-aminobutyric acid, and indomethacin) were used to investigate their potential effects on sodium and hERG potassium ion channels in bioengineered cardiac constructs. The effect of the drugs on

intracellular Na^+ levels was monitored using the Na^+ indicator. Similarly, the effect of the drugs on the hERG potassium ion channel was measured using the FluxOR™ potassium channel assay and immunofluorescence staining. An increase in drug concentration resulted in a decrease in K^+ permeability and intracellular Na^+ level. Therefore, a lower number of Na^+− and K^+−indicator−positive fluorescent cells was observed in the groups treated with digoxin, cisapride, and IMC than in the control without drug treatment. In contrast, GABA showed no significant effect on K^+ channel blockade over the range of concentrations tested. K^+ channel permeability and hERG immunofluorescence remained almost the same in treated cells as in the control over the entire drug range tested. Thus, intracellular homeostasis was well preserved in the GABA−treated cardiac construct. The results of the current study are therefore of great value as they demonstrate that the SFP−based bioengineered cardiac constructs used are capable of responding to changes in membrane potential and can therefore be used as a novel platform for screening small molecule−induced blockade of Na^+ and hERG−K^+ channels.

Further investigations for the use of the SFP−based bioengineered cardiac constructs for identification of nanomaterial−induced blockade of Na^+ and hERG−K^+ channels is necessary. Previously, Triphenylphosphine (TPP)−stabilized AuNPs have been reported to irreversibly block the permeability of K^+ channels using 2D cell culture, whereas thiol−stabilized AuNPs of similar sizes had no such effect *in vitro* [54]. Thus, the potential hazards of surface−functionalized AuNPs are an important issue that warrants further investigation. Particularly, the absence of hERG K^+ channel blockage caused by anticancer materials conjugated onto the surface of AuNPs,

has to be demonstrated for the successful development of nanomaterials. Size-dependent hERG potassium channel blockage is another factor to be considered with respect to the nanomaterials because inhibition of K^+ permeation in K^+ channels can occur because of the binding of nanomaterials to hERG proteins as a function of their size.

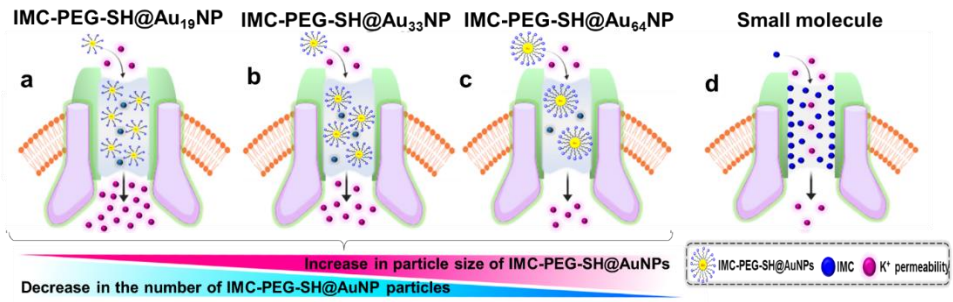

Figure 19. Schematic illustration of size-dependent binding of IMC-PEG-SH@AuNPs to hERG proteins vs. binding of IMC (small molecule) to hERG proteins.

In the present study, IMC-PEG-SH@AuNPs with sizes of 19 nm, 33 nm, and 64 nm were synthesized, and their size-dependent effects on hERG K^+ channels were evaluated for the first time. Figure 17 clearly shows that the largest AuNPs (~ 64 nm) caused the largest hERG channel blockage. The three different sizes of spherical IMC-PEG-SH@AuNPs have different surface areas. The number of surface ligands IMC-PEG-SH bound to the surface of AuNPs increased as the size of AuNPs increased because the surface area of larger AuNPs increased. The concentration of the surface ligand IMC-PEG-SH conjugated to the surface of AuNPs was quantitatively determined using absorption spectra. Consequently, three different sizes of IMC-PEG-SH@AuNPs with identical surface ligand concentrations were prepared, and the size-dependent hERG

channel blockage of AuNPs was determined under the condition that the three different sizes of IMC-PEG-SH@AuNPs had the same probability of being bound to hERG proteins in the K^+ channel. When the concentration of the surface ligand IMC-PEG-SH was the same for the three different sizes of IMC-PEG-SH@AuNPs, the number of the largest IMC-PEG-SH@AuNPs was the smallest because the number of ligands IMC-PEG-SH bound to the surface of the AuNPs had to be the largest for the largest AuNPs, as shown in Figure 19. Considering that the binding of IMC-PEG-SH@AuNPs to hERG proteins is achieved not by AuNPs but by surface ligands, and the concentration of surface ligands is identical in all three IMC-PEG-SH@AuNPs, the number of IMC-PEG-SH@AuNPs bound to hERG proteins in the K^+ channel should be the largest for the smallest IMC-PEG-SH@AuNPs (19 nm) under the same surface ligand concentration. Notably, the largest IMC-PEG-SH@AuNPs (64 nm) induced the largest hERG channel blockage, despite the smallest number bound to hERG proteins in the K^+ channel. This signifies that hERG protein binding induced by nanomaterials is more dependent on the size than on the number of nanoparticles.

To further validate the influence of nanomaterial surface functionalization on hERG protein binding in K^+ channels, F-108@TPP-AuNPs were tested using the *in-situ* 3D bioengineered cardiac model. Although the F-108@TPP-AuNPs, with sizes of ~10 nm, are smaller than IMC-PEG-SH@Au_{19}NPs, K^+ permeation was inhibited more strongly with F-108@TPP-AuNPs than with IMC-PEG-SH@Au_{19}NPs. This difference could be attributed to the difference in the binding activity of surface ligands to hERG proteins.

Another important finding of the present study is that nanomaterial-induced hERG channel blockage is less severe than that induced by small molecules. Of all the ligands attached to a single spherical AuNP, only some ligands directed to the hERG proteins in the hERG K^+ channel can be bound to them because of the steric restriction in the approach of surface ligands on AuNPs to hERG proteins. In contrast, small molecules do not have such steric restrictions for binding to hERG proteins in the K^+ channel. As a result, more opportunities for binding to hERG proteins in K^+ channels are created for small molecules. This is the first study to demonstrate that nanomaterials may have a lower hERG channel blockage than small molecules.

Conclusion

In summary, we have developed a scaffold-free de novo printing (SFP)-based matrix that models the ECM networks of native myocardium. By varying the adhesive ligand, architecture, and mechanics of these matrices, we found that sodium alginate and gelatin, together with fibrinogen and growth hormones, facilitated the formation of organized cardiomyocyte tissue layers. Our results support the notion that the SFP method together with fibrin-based ECM is sufficient to generate cardiac tissues with native tissue-like phenotypes. The 3D cardiac cells produced by SFP achieved high confluence with a branched cell structure with many nuclei. Moreover, the formation of tight intracellular junctions expressing connexin 43 confirms the maturation of the fabricated structure. Interestingly, the effect of small molecules on the sodium and potassium ion channels proves that this analytical method can be used for drug screening and new drug discovery due to its high predictability of drug action in vitro. Moreover, fabricated 3D cardiac constructs were successfully used to monitor the dose-dependent reduction of K^+ permeation and hERG protein expression by nanomaterials. Overall, the results of this dissertation can be summarized as follows: 1. nanomaterials with two different surface ligands (IMC-PEG-SH @AuNPs and F-108@TPP-AuNPs) showed a dose-dependent decrease in K^+ permeation due to their binding to hERG proteins; 2. the extent of hERG K^+ channel blockade was dependent on the surface ligand conjugated to the AuNPs. 3. In the same way, the size-dependent effect of the nanomaterials on hERG K^+ channel blockade was quantitatively evaluated using the three different sizes of IMC-PEG-SH @AuNPs. The effect of K^+ channel blockade was remarkably

proportional to the size of the IMC-PEG-SH @AuNPs. 4. It was also observed that binding of small molecules greatly reduced K^+ permeation and hERG immunofluorescence compared with IMC-PEG-SH @AuNPs, which may be due to steric limitations in binding of surface ligands to hERG proteins. Therefore, the proposed SFP-based bioprinted 3D constructs for the heart, which allow fluorescence-based measurement of the membrane potential of Na^+ and K^+ channels, can be used as a screening tool to measure ion channel blockage induced by nanomaterials to small molecules.

Acknowledgement

My journey to complete this dissertation has been quite long and strenuous. I would like to express my deepest gratitude to all the people who helped me complete this dissertation.

I would like to thank my doctoral advisor Joon Myong Song for entrusting me with this project, for helping me with various problems, for giving me interesting suggestions about my work, and for supporting me throughout my doctoral studies. The fact that I was able to complete my dissertation is due to the help of many other people, whom I would like to thank at this point. I am immensely grateful to my collaborator Sera Hong (my little sister from another mother). Without your help, I would not have been able to complete my projects so efficiently. I will remember all of our activities, our lunch conversations, our shared love of K-dramas, and our stimulating discussions. I am glad to have met you and wish you all the best in life. I would like to thank all the current and former members of the group, including Ju Hee, Nam Gee woo, Solji Park, Jinran Lee, Parthasarathi, Goutham Kulsi, Baskaran, Sandip Balwe, and Ayman. My friends outside of work, Nisha and Shruthi, thank you for all the love and encouragement.

My family has been a pillar of support, guiding me through many difficult situations in life. I would like to thank my mother (Sebasti Christina Nithila) and father (Samson) for their love, appreciation and belief in me. My gratitude to my mother-in-law (Victoria Mary) and father-in-law (John Joseph) cannot be expressed in words. Thank you for your unwavering support. To my brother (Dr. Jegan Jennifer) and sister-in-law (Nancy), you have been an invaluable support in

my life and I admire you both for who you are. It has been a blessing to me to see you struggle with a positive attitude. I have learned from your example how to deal with problems that seem "insurmountable". And finally, I want to thank one of the most important parts of my life, my partner Wilson. Thank you for sticking with me through the difficult times. I could not have done it without you and our lucky little kid, Steve Austin. This work is dedicated to my children (Steve Austin, Sam Rickson and Sara Jerslin). You have made me stronger, better and more fulfilled than I could have ever imagined. I love you guys to the moon and back.

Bibliography

1. Mironov V, Reis N, Derby B. Review: bioprinting: a beginning. Tissue Eng. 2006 Apr;12(4):631-4.
2. Klebe RJ. Cytoscribing: a method for micropositioning cells and the construction of two- and three-dimensional synthetic tissues. Exp Cell Res. 1988 Dec;179(2):362-73.
3. Wilson WC Jr, Boland T. Cell and organ printing 1: protein and cell printers. Anat Rec A Discov Mol Cell Evol Biol. 2003 Jun;272(2):491-6.
4. Smith CM, Stone AL, Parkhill RL, Stewart RL, Simpkins MW, Kachurin AM, Warren WL, Williams SK. Three-dimensional bioassembly tool for generating viable tissue-engineered constructs. Tissue Eng. 2004 Sep-Oct;10(9-10):1566-76.
5. Murphy SV, Atala A. 3D bioprinting of tissues and organs. Nat Biotechnol. 2014 Aug;32(8):773-85.
6. Smith CM, Stone AL, Parkhill RL, Stewart RL, Simpkins MW, Kachurin AM, Warren WL, Williams SK. Three-dimensional bioassembly tool for generating viable tissue-engineered constructs. Tissue Eng. 2004 Sep-Oct;10(9-10):1566-76.
7. Schuurman W, Levett PA, Pot MW, van Weeren PR, Dhert WJ, Hutmacher DW, Melchels FP, Klein TJ, Malda J. Gelatin-methacrylamide hydrogels as potential biomaterials for fabrication of tissue-engineered cartilage constructs. Macromol Biosci. 2013 May;13(5):551-61.
8. Xu M, Wang X, Yan Y, Yao R, Ge Y. An cell-assembly derived physiological 3D model of the metabolic syndrome, based on adipose-derived stromal cells and a

gelatin/alginate/fibrinogen matrix. Biomaterials. 2010 May;31(14):3868-77.

9. Bracaglia LG, Fisher JP. Extracellular Matrix-Based Biohybrid Materials for Engineering Compliant, Matrix-Dense Tissues. Adv Healthc Mater. 2015 Nov 18;4(16):2475-87.
10. Del Bakhshayesh, A.R., Asadi, N., Alihemmati, A. et al. An overview of advanced biocompatible and biomimetic materials for creation of replacement structures in the musculoskeletal systems: focusing on cartilage tissue engineering. J Biol Eng 13, 85 (2019).
11. WonJin Kim, GeunHyung Kim, 3D bioprinting of functional cell-laden bioinks and its application for cell-alignment and maturation, Applied Materials Today, Volume 19, 2020, 100588.
12. Lee, H.N., Choi, Y.Y., Kim, J.W. et al. Effect of biochemical and biomechanical factors on vascularization of kidney organoid-on-a-chip. Nano Convergence 8, 35 (2021).
13. Nicolas J, Magli S, Rabbachin L, Sampaolesi S, Nicotra F, Russo L. 3D Extracellular Matrix Mimics: Fundamental Concepts and Role of Materials Chemistry to Influence Stem Cell Fate. Biomacromolecules. 2020 Jun 8;21(6):1968-1994.
14. K.Y. Ye, K.E. Sullivan, L.D. Black, Encapsulation of cardiomyocytes in a fibrin hydrogel for cardiac tissue engineering, J. Vis. Exp. (2011) 3251.
15. W.R. Legant, A. Pathak, M.T. Yang, V.S. Deshpande, R.M. McMeeking, C.S. Chen, Microfabricated tissue gauges to measure and manipulate forces from 3D microtissues, Proc. Natl. Acad. Sci. 106 (2009) 10097-10102.

16. M.L. McCain, A. Agarwal, H.W. Nesmith, A.P. Nesmith, K.K. Parker, Micromolded gelatin hydrogels for extended culture of engineered cardiac tissues, Biomaterials. 35 (2014) 5462–5471.
17. J.M. Singelyn, J.A. DeQuach, S.B. Seif-Naraghi, R.B. Littlefield, P.J. SchupMagoffin, K.L. Christman, Naturally derived myocardial matrix as an injectable scaffold for cardiac tissue engineering, Biomaterials. 30 (2009) 5409–5416.
18. F. Pati, J. Jang, D.-H. Ha, S. Won Kim, J.-W. Rhie, J.-H. Shim, D.-H. Kim, D.-W. Cho, Printing three-dimensional tissue analogues with decellularized extracellular matrix bioink, Nat. Commun. 5 (2014) 3935.
19. M.N. Hirt, A. Hansen, T. Eschenhagen, Cardiac tissue engineering: State of the art, Circ. Res. 114 (2014) 354–367.
20. Jang J, Park HJ, Kim SW, Kim H, Park JY, Na SJ, Kim HJ, Park MN, Choi SH, Park SH, Kim SW, Kwon SM, Kim PJ, Cho DW. 3D printed complex tissue construct using stem cell-laden decellularized extracellular matrix bioinks for cardiac repair. Biomaterials. 2017 Jan;112:264-274.
21. Park, SJ., Kim, R.Y., Park, BW. et al. Dual stem cell therapy synergistically improves cardiac function and vascular regeneration following myocardial infarction. Nat Commun 10, 3123 (2019).
22. Das S, Kim SW, Choi YJ, Lee S, Lee SH, Kong JS, Park HJ, Cho DW, Jang J. Decellularized extracellular matrix bioinks and the external stimuli to enhance cardiac tissue development in vitro. Acta Biomater. 2019 Sep 1;95:188-200.

23. Beauchamp P, Jackson CB, Ozhathil LC, Agarkova I, Galindo CL, Sawyer DB, Suter TM, Zuppinger C. 3D Co-culture of hiPSC-Derived Cardiomyocytes With Cardiac Fibroblasts Improves Tissue-Like Features of Cardiac Spheroids. Front Mol Biosci. 2020 Feb 14;7:14.
24. Ong, C. S., Fukunishi, T., Nashed, A., Blazeski, A., Zhang, H., Hardy, S., DiSilvestre, D., Vricella, L., Conte, J., Tung, L., Tomaselli, G., Hibino, N. Creation of Cardiac Tissue Exhibiting Mechanical Integration of Spheroids Using 3D Bioprinting. J. Vis. Exp. (125), e55438, doi:10.3791/55438 (2017).
25. Al-Dhahebi, A.M., Gopinath, S.C.B. & Saheed, M.S.M. Graphene impregnated electrospun nanofiber sensing materials: a comprehensive overview on bridging laboratory set-up to industry. Nano Convergence 7, 27 (2020).
26. Kang, S., Park, S.E. & Huh, D.D. Organ-on-a-chip technology for nanoparticle research. Nano Convergence 8, 20 (2021).
27. Chen, L.; Sampson, K. J.; Kass, R. S., Cardiac Delayed Rectifier Potassium Channels in Health and Disease. Card. Electrophysiol. Clin. 2016, 8 (2), 307-22.
28. Priest, B. T.; Bell, I. M.; Garcia, M. L., Role of hERG potassium channel assays in drug development. Channels 2008, 2 (2), 87-93.
29. Shi, Y. P.; Thouta, S.; Claydon, T. W., Modulation of hERG K(+) Channel Deactivation by Voltage Sensor Relaxation. Front Pharmacol 2020, 11, 139.
30. Vandenberg, J. I.; Perry, M. D.; Perrin, M. J.; Mann, S. A.; Ke, Y.; Hill, A. P., hERG K(+) channels: structure, function, and clinical significance. Physiol Rev 2012, 92 (3), 1393-478.

31. Redfern, W. S.; Carlsson, L.; Davis, A. S.; Lynch, W. G.; MacKenzie, I.; Palethorpe, S.; Siegl, P. K.; Strang, I.; Sullivan, A. T.; Wallis, R.; Camm, A. J.; Hammond, T. G., Relationships between preclinical cardiac electrophysiology, clinical QT interval prolongation and torsade de pointes for a broad range of drugs: evidence for a provisional safety margin in drug development. *Cardiovas res.* 2003, *58* (1), 32-45.
32. Mamoshina, P.; Rodriguez, B.; Bueno-Orovio, A., Toward a broader view of mechanisms of drug cardiotoxicity. *Cell reports. Med* 2021, *2* (3), 100216.
33. Grilo, L. S.; Carrupt, P. A.; Abriel, H., Stereoselective Inhibition of the hERG1 Potassium Channel. *Front Pharmacol* 2010, *1*, 137.
34. Yu, H. B.; Li, M.; Wang, W. P.; Wang, X. L., High throughput screening technologies for ion channels. *Acta pharmacol Sinica* 2016, *37* (1), 34-43.
35. Titus, S. A.; Beacham, D.; Shahane, S. A.; Southall, N.; Xia, M.; Huang, R.; Hooten, E.; Zhao, Y.; Shou, L.; Austin, C. P.; Zheng, W., A new homogeneous high-throughput screening assay for profiling compound activity on the human ether-a-go-go-related gene channel. *Anal biochem* 2009, *394* (1), 30-8.
36. Huang, X. P.; Mangano, T.; Hufeisen, S.; Setola, V.; Roth, B. L., Identification of human Ether-à-go-go related gene modulators by three screening platforms in an academic drug-discovery setting. *Assay Drug Dev Technol* 2010, *8* (6), 727-42.

37. Langhans, S. A., Three-Dimensional in Vitro Cell Culture Models in Drug Discovery and Drug Repositioning. *Front Pharmacol* 2018, *9*, 6.
38. Jensen, C.; Teng, Y., Is It Time to Start Transitioning From 2D to 3D Cell Culture? *Front. Mol. Biosci.* 2020, *7*, 33.
39. Chaicharoenaudomrung, N.; Kunhorm, P.; Noisa, P., Three-dimensional cell culture systems as an in vitro platform for cancer and stem cell modeling. *World J Stem Cells* 2019, *11* (12), 1065-1083.
40. Hu, X.; Zhang, Y.; Ding, T.; Liu, J.; Zhao, H., Multifunctional Gold Nanoparticles: A Novel Nanomaterial for Various Medical Applications and Biological Activities. *Front Bioeng Biotechnol* 2020, *8*, 990.
41. Li, W.; Cao, Z.; Liu, R.; Liu, L.; Li, H.; Li, X.; Chen, Y.; Lu, C.; Liu, Y., AuNPs as an important inorganic nanoparticle applied in drug carrier systems. *Artif. Cells Nanomed. Biotechnol.* 2019, *47* (1), 4222-4233.
42. Riley, R. S.; Day, E. S., Gold nanoparticle-mediated photothermal therapy: applications and opportunities for multimodal cancer treatment. *Nanomed Nanobiotech* 2017, *9* (4).
43. Cheheltani, R.; Ezzibdeh, R. M.; Chhour, P.; Pulaparthi, K.; Kim, J.; Jurcova, M.; Hsu, J. C.; Blundell, C.; Litt, H. I.; Ferrari, V. A.; Allcock, H. R.; Sehgal, C. M.; Cormode, D. P., Tunable, biodegradable gold nanoparticles as contrast agents for computed tomography and photoacoustic imaging. *Biomaterials* 2016, *102*, 87-97.

44. Miao, Y.; Yang, T.; Yang, S.; Yang, M.; Mao, C., Protein nanoparticles directed cancer imaging and therapy. *Nano Converg* 2022, *9* (1), 2.
45. Byun, H.; Jang, G.N.; Hong, MH.; Yeo, J.; Shin, H.; Kim, W. J.; Shin, H., Biomimetic anti-inflammatory and osteogenic nanoparticles self-assembled with mineral ions and tannic acid for tissue engineering. *Nano Converg.* 2022, *9*, 47.
46. Kim, J.Y.; Rhim, WK.; Cha, SG.; Woo, J.; Lee, J. Y.; Park, C. G.; Han, D. K., Bolstering the secretion and bioactivities of umbilical cord MSC-derived extracellular vesicles with 3D culture and priming in chemically defined media. *Nano Converg.* 2022, *9*, 57.
47. Kalogianni, D. P., Nanotechnology in emerging liquid biopsy applications. *Nano Converg* 2021, *8* (1), 13.
48. Rosa, S.; Connolly, C.; Schettino, G.; Butterworth, K. T.; Prise, K. M., Biological mechanisms of gold nanoparticle radiosensitization. *Cancer nanotechnol* 2017, *8* (1), 2.
49. Guo, S.; Huang, Y.; Jiang, Q.; Sun, Y.; Deng, L.; Liang, Z.; Du, Q.; Xing, J.; Zhao, Y.; Wang, P. C.; Dong, A.; Liang, X. J., Enhanced gene delivery and siRNA silencing by gold nanoparticles coated with charge-reversal polyelectrolyte. *ACS Nano* 2010, *4* (9), 5505-11.
50. Amina, S. J.; Guo, B., A Review on the Synthesis and Functionalization of Gold Nanoparticles as a Drug Delivery Vehicle. *Int J Nanomedicine* 2020, *15*, 9823-9857.
51. Senapati, S.; Mahanta, A. K.; Kumar, S.; Maiti, P., Controlled drug delivery vehicles for cancer treatment and their performance. *Signal Transduct. Target. Ther.* 2018, *3*, 7.

52. Pivodová, V.; Franková, J.; Galandáková, A.; Ulrichová, J., In Vitro AuNPs' Cytotoxicity and Their Effect on Wound Healing. *Nanobiomed* 2015, *2*, 7.
53. Kus-Liśkiewicz, M.; Fickers, P.; Ben Tahar, I., Biocompatibility and Cytotoxicity of Gold Nanoparticles: Recent Advances in Methodologies and Regulations. *Int J Mol Sci* 2021, *22* (20).
54. Leifert, A.; Pan, Y.; Kinkeldey, A.; Schiefer, F.; Setzler, J.; Scheel, O.; Lichtenbeld, H.; Schmid, G.; Wenzel, W.; Jahnen-Dechent, W.; Simon, U., Differential hERG ion channel activity of ultrasmall gold nanoparticles. *Proc. Natl. Acad. Sci.* 2013, *110* (20), 8004-9.
55. Bastús, N. G.; Comenge, J.; Puntes, V., Kinetically controlled seeded growth synthesis of citrate-stabilized gold nanoparticles of up to 200 nm: size focusing versus Ostwald ripening. *Langmuir* 2011, *27* (17), 11098-105.
56. Lee, E.; Jeon, H.; Lee, M.; Ryu, J.; Kang, C.; Kim, S.; Jung, J.; Kwon, Y., Molecular origin of AuNPs-induced cytotoxicity and mechanistic study. *Sci Rep* 2019, *9* (1), 2494.
57. Heo, J. H.; Kim, K. I.; Cho, H. H.; Lee, J. W.; Lee, B. S.; Yoon, S.; Park, K. J.; Lee, S.; Kim, J.; Whang, D.; Lee, J. H., Ultrastable-Stealth Large Gold Nanoparticles with DNA Directed Biological Functionality. *Langmuir* 2015, *31* (51), 13773-82.
58. Benyettou, F.; Ramdas Nair, A.; Dho, Y.; Prakasam, T.; Pasricha, R.; Whelan, J.; Traboulsi, H.; Mazher, J.; Sadler, K. C.; Trabolsi, A., Aqueous Synthesis of Triphenylphosphine-Modified Gold Nanoparticles for

Synergistic In Vitro and In Vivo Photothermal Chemotherapy. *Chemistry* 2020, *26* (23), 5270-5279.

59. Hong, S., and Song, J. M., A 3D cell printing-fabricated HepG2 liver spheroid model for high-content in situ quantification of drug-induced liver toxicity. *Biomater Sci* (2021) 9 (17), 5939
60. Coffin ST, Gaudette GR. Aprotinin extends mechanical integrity time of cell-seeded fibrin sutures. J Biomed Mater Res A. 2016 Sep;104(9):2271-9.
61. Antich C, de Vicente J, Jiménez G, Chocarro C, Carrillo E, Montañez E, Gálvez-Martín P, Marchal JA. Bio-inspired hydrogel composed of hyaluronic acid and alginate as a potential bioink for 3D bioprinting of articular cartilage engineering constructs. Acta Biomater. 2020 Apr 1;106:114-123.
62. Wang, Z.; Lee, S. J.; Cheng, H. J.; Yoo, J. J.; Atala, A., 3D bioprinted functional and contractile cardiac tissue constructs. *Acta Biomater* 2018, *70*, 48-56.
63. Nam, K. H.; Smith, A. S.; Lone, S.; Kwon, S.; Kim, D. H., Biomimetic 3D Tissue Models for Advanced High-Throughput Drug Screening. *J. Lab. Autom.* 2015, *20* (3), 201-15.
64. Jorba, I.; Mostert, D.; Hermans, L. H. L.; van der Pol, A.; Kurniawan, N. A.; Bouten, C. V. C., In Vitro Methods to Model Cardiac Mechanobiology in Health and Disease. *Tissue Eng. Part C Methods* 2021, *27* (3), 139-151.

Abstract in Korean

현재 약물 발견은 치료에 대한 생리학적 반응을 정확하게 반영하지 못하는 부적절한 모델로 인해 방해를 받고 있습니다. 최근 몇 가지 약물이 효능 부족 또는 임상 시험 중에 발견되지 않은 예상치 못한 부작용, 특히 심장 독성으로 인해 시장에서 철수되었습니다. 이 논문의 주요 목적은 나트륨 및 칼륨 이온 채널의 약물 유발 차단을 연구하기 위해 스캐폴드가 없는 3D 프린팅(SFP) 생체 모방 심장 조직 구조를 개발하는 것입니다. 이 작업에서는 비계가 없는 3D 인쇄(SFP) 모델이라는 3D 인쇄 기술을 사용하여 하이드로겔에 쥐 배아 심근세포(H9C2)를 빠르고 공간적으로 배열했습니다. 바이오잉크의 제형을 변경하고 심근세포를 특정 마이크로아키텍처에 내장함으로써, 심근세포는 설계된 기하학과 우선적으로 정렬되고 네이티브 조직 유사 표현형과 유사한 다핵 세포가 있는 분지형 세포 구조를 가진 생체모방 심장 조직으로 재생됩니다. SFP 로 조작된 3D 심장 세포는 여러 개의 핵을 가진 분지형 세포 구조로 높은 합류를 달성했습니다. connexin 43 을 발현하는 단단한 세포내 접합부의 형성은 조작된 구조의 성숙을 확인했습니다. 이 접근법을 사용하여 심장 조직 구조물을 성공적으로 제작하고 나트륨 및 칼륨 이온 채널 반응을 측정하기에 충분히 민감한 분석 플랫폼으로 사용했습니다.

처음에 이 연구는 알려진 심장 약물에 대한 생체 공학 심장 구조물의 생리학적 나트륨 및 칼륨 이온 채널 반응의 현장 측정에 초점을 맞췄습니다. 다양한 소분자를 사용하여 SFP 로 조작된 3D 심장 조직 구조물이 시험관 내 약물 반응의 높은 예측 가능성으로 인해 스크리닝 및 약물 발견에 사용될 수 있음이 입증되었습니다. 다음으로 우리는 나노 물질에 의한 hERG(human ether−à−go−go−related) 유전자 칼륨 채널의 크기 의존적 차단을 스크리닝하기 위한 SFP 조작 3D 심장 조직 구조물의 민감도를 조사했습니다. 이 목표를 달성하기 위해 크기와 표면 리간드가 다른 금 나노 입자를 합성하고 3D 생체 모방 심장 조직 모델을 사용하

여 칼륨 이온 채널 투과성 및 hERG 단백질 면역 형광을 모니터링하여 hERG 칼륨 채널의 크기 및 표면 리간드 의존적 차단을 고유하게 측정했습니다. . 우리의 결과는 나트륨 및 칼륨 이온 채널의 막 전위에 대한 형광 기반 측정을 허용하는 제안된 SFP 기반 생체 인쇄 3D 심장 구조가 나노 물질에 의한 이온 채널 차단을 측정하는 스크리닝 도구로 사용될 수 있음을 시사합니다. 작은 분자에.

Supporting Information

Scheme S1. Synthesis route of IMC−PEG−SH (4)

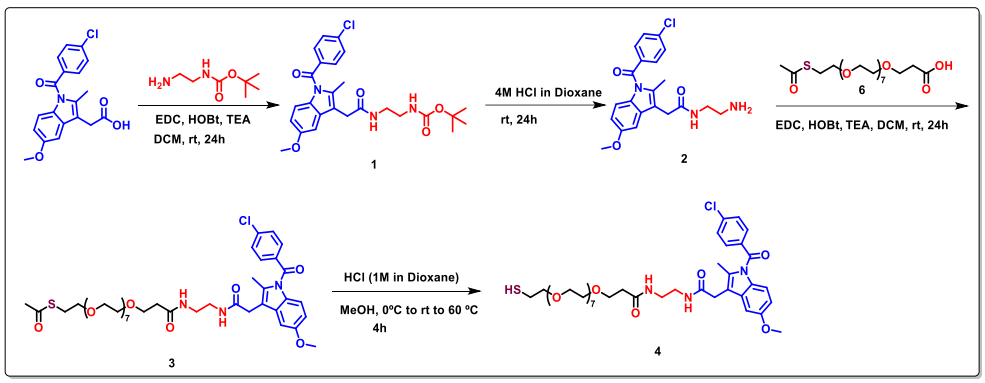

Compound 1

To a stirred solution of indomethacin (0.5 g, 1.40 mmol) in DCM (15 mL), EDC•HCl (0.349 g, 1.82 mmol), and HOBt (0.246 g, 1.82 mmol) was added and mixture was stirred at room temperature for 15 min. *tert*−Butyl *N*−(2−aminoethyl)carbamate (0.246 g, 1.54 mmol) and TEA (0.58 ml, 4.20 mmol) were added and resulting mixture was stirred overnight. Water (15 mL) was added to the reaction mixture and aqueous solution was extracted with DCM (3 X 20 mL). The organic layer was separated and washed with brine, dried over anhydrous sodium sulfate, filtered and evaporated under reduced pressure. The crude mixture was purified by column chromatography using silica gel with a eluant gradient of 2−3% MeOH in DCM to obtain compound **1** as white solid (0.59 g, yield 84 %). ^{1}H NMR (400 MHz, $CDCl_3$): δ 7.70 (d, J = 8.6 Hz, 2H), 7.48 (d, J = 8.6 Hz, 2H), 6.89 (dd, J = 5.8, 3.2 Hz, 2H), 6.69 (dd, J = 9.1, 2.5 Hz, 1H), 6.29 (s, 1H), 4.80 (s, 1H), 3.82 (s, 3H), 3.63 (s, 2H), 3.34 – 3.28 (m, 2H), 3.21 – 3.15 (m, 2H), 2.38 (s, 3H), 1.34 (s, 9H). ^{13}C NMR (100 MHz, $CDCl_3$): δ 170.81, 168.46, 156.40, 136.50, 131.37, 131.07,

129.33, 115.34, 112.87, 112.39, 100.81, 79.89, 55.88, 41.21, 40.64, 32.36, 28.39, 13.49.

Compound 2

To a stirred solution of compound *tert*-butyl (2-(2-(1-(4-chlorobenzoyl)-5-methoxy-2-methyl-1*H*-indol-3-yl)acetamido)ethyl)carbamate **1** (0.590 g, 1.18 mmol) in DCM (20 mL), 4M HCl in dioxane (4 mL) was added and mixture was stirred under an inert atmosphere overnight. After completion, the mixture was evaporated under reduced pressure to obtain compound **2**. The HCl salt of *N*-(2-aminoethyl)-2-(1-(4-chlorobenzoyl)-5-methoxy-2-methyl-1*H*-indol-3-yl)acetamide appeared as an off-white solid (0.34 g, yield 72%). ^{1}H NMR (400 MHz, DMSO-d_6): δ 8.60 (t, J = 5.5 Hz, 1H), 8.23 (s, 2H), 7.72 - 7.61 (m, 4H), 7.20 (d, J = 2.5 Hz, 1H), 6.93 (d, J = 9.0 Hz, 1H), 6.70 (dd, J = 9.0, 2.5 Hz, 1H), 3.78 (s, 3H), 3.57 (s, 2H), 3.36 - 3.29 (m, 2H), 2.90 - 2.82 (m, 2H), 2.25 (s, 3H). ^{13}C NMR (100 MHz, DMSO-d_6): δ 169.91, 167.69, 155.41, 137.39, 135.11, 134.07, 131.02, 130.71, 130.05, 128.88, 114.37, 113.93, 111.17, 101.78, 55.41, 36.43, 30.93, 13.32.

Compound 3

To a solution of compound **2** (0.108 g, 0.247 mmol) in DMF (5 mL), EDC•HCl (0.062 g, 0.322 mmol), and HOBt (0.044 g, 0.322 mmol) were added and mixture was stirred at room temperature for 15 min. Compound **7** (0.114 g, 0.247 mmol) and TEA (0.103 ml, 0.743 mmol) were added and resulting mixture was stirred overnight. After completion, the mixture was diluted with CH_2Cl_2 (50 mL), washed with aqueous sodium bicarbonate (10 mL X 3). The combined organic extract was separated and washed with brine, dried over anhydrous

sodium sulfate, filtered and evaporated under reduced pressure. The crude mixture was purified by flash column chromatography using silica gel with an eluent gradient of 3 % MeOH/CH_2Cl_2 to obtain compound **3** as off-white solid (0.118 g, yield 54 %). ^{1}H NMR (400 MHz, $CDCl_3$): δ 7.77 (d, J = 8.4 Hz, 2H), 7.45 (d, J = 8.4 Hz, 2H), 7.02 (s, 1H), 6.91 – 6.83 (m, 2H), 6.79 (s, 1H), 6.64 (dd, J = 9.0, 2.4 Hz, 1H), 3.80 (s, 3H), 3.65 – 3.54 (m, 32H), 3.52 – 3.46 (m, 4H), 3.29 (s, 4H), 3.06 (t, J = 6.5 Hz, 2H), 2.36 (s, 3H), 2.31 (s, 3H), 2.19 (t, J = 5.5 Hz, 2H). ^{13}C NMR (100 MHz, $CDCl_3$): δ 195.66, 173.24, 170.91, 168.52, 156.14, 139.29, 136.54, 134.01, 131.46, 131.13, 130.71, 129.16, 115.14, 112.91, 111.87, 101.00, 70.55, 70.32, 69.81, 66.96, 55.81, 41.58, 38.59, 36.40, 32.19, 30.67, 29.77, 28.88, 13.40.

Compound 4

To a MeOH solution (5 mL) of compound **3** (0.118 g, 0.133 mmol), 1N HCl (0.5 mL) was added under Ar, and mixture was refluxed for 4 h at 80 ºC. Then, water (4 mL) was added to the resulting solution, and the mixture was extracted with CH_2Cl_2 (10 mL X 3). The organic layer was separated and dried over anhydrous sodium sulfate, filtered and evaporated under reduced pressure. The residue was chromatographed on silica gel with 5% MeOH/ CH_2Cl_2 as an eluent to obtain compound **4** as white solid (0.068 g, yield 60 %). ^{1}H NMR (400 MHz, $CDCl_3$): δ 7.78 (d, J = 8.5 Hz, 2H), 7.46 (d, J = 8.5 Hz, 2H), 7.04 (s, 1H), 6.90 – 6.83 (m, 2H), 6.77 (s, 1H), 6.64 (dd, J = 9.0, 2.5 Hz, 1H), 3.80 (s, 3H), 3.66 – 3.58 (m, 32H), 3.57 – 3.54 (m, 2H), 3.53 – 3.45 (m, 4H), 3.30 (s, 4H), 2.74 – 2.63 (m, 2 H), 2.37 (s, 3H), 2.20 (t, J = 5.6 Hz, 2H), 1.58 (t, J = 8.2 Hz, 1H). ^{13}C NMR (100 MHz, $CDCl_3$): δ 172.22, 169.84, 167.42, 155.05, 138.21,

135.47, 132.91, 130.37, 130.04, 129.59, 129.51, 128.06, 114.06, 111.75, 110.79, 99.88, 71.84, 69.49, 69.19, 69.10, 69.00, 65.84, 54.72, 40.53, 37.50, 35.27, 31.10, 23.25, 12.30. HR-MS found: m/z: 857.3752 $[M+NH_4]^+$, calcd for $C_{40}H_{58}ClN_3O_{12}S$, 839.3415.

Synthesis of Compound 6

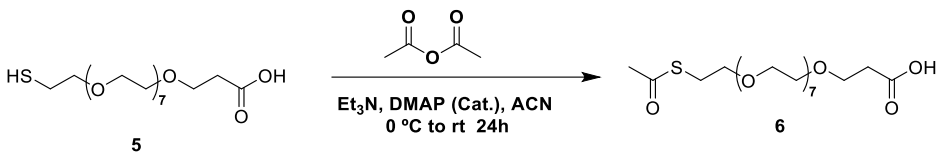

The compound **6** was synthesized by using commercially available 1-mercapto-3,6,9,12,15,18,21,24-octaoxaheptacosan-27-oic acid (compound **5**). Acetic anhydride (1.1 equiv.) was added dropwise at 0 ºC to a solution of compound **5** (1.0 equiv.), triethylamine (2 equiv.), and catalytic amount of DMAP in anhydrous acetonitrile. The reaction mixture was stirred at room temperature for 24 h. Then, the solvent was evaporated to dryness, and the residue was quenched with water. The aqueous layer was washed with diethyl ether, acidified to pH = 1 by the addition of aqueous 1N HCl solution, and extracted with ethyl acetate. The combined organic phases were washed with brine, dried over anhydrous sodium sulfate, filtered and evaporated under reduced pressure to afford compound **6** as a pale yellow oil. ^{1}H NMR (400 MHz, DMSO-d_6): δ 3.62 - 3.57 (m, 2H), 3.52 - 3.49 (m, 23H), 3.49 - 3.48 (m, 3H), 3.01 (t, J = 6.5 Hz, 2H), 2.43 (t, J = 6.3 Hz, 2H), 2.33 (s, 3H). ^{13}C NMR (100 MHz, DMSO-d_6): δ 195.18, 172.69, 69.81, 69.72, 69.65, 69.59, 68.93, 66.26, 34.77, 30.54, 28.29.

Scheme S2. AuNPs surface modification via a ligand exchange reaction

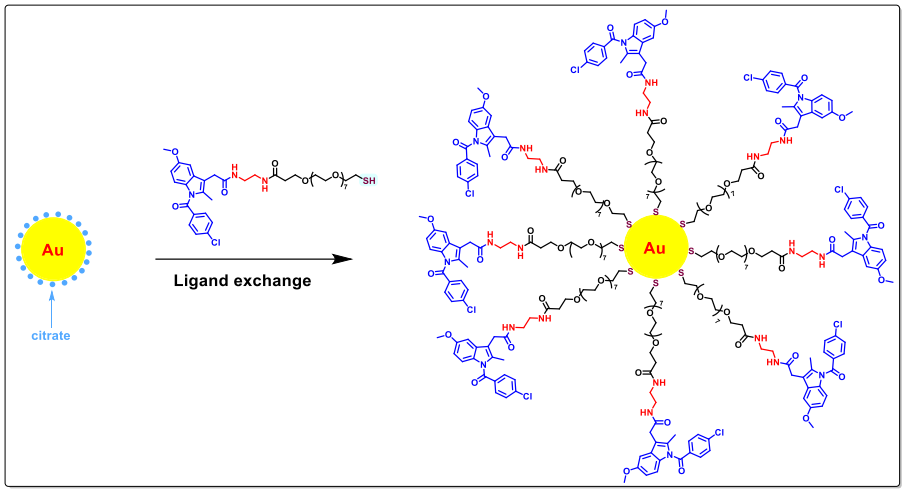

Table S1. Physicochemical characterization of different sizes of AuNPs

AuNPs	TEM diameter (nm)	SPR peak (nm)	Hydrodynamic diameter (nm)	Zeta potential (mV)
Au_9NPs	9.2 ± 1.8	521	10.6 ± 0.4	−34.9
Au_{17}NPs	17.4± 2.3	524	18.9 ± 0.3	−38.0
Au_{46}NPs	45.7± 5.8	530	46.8 ± 0.1	−46.5

Table S2. Physicochemical characterization of different sizes of IMC−PEG−SH@AuNPs

IMC−PEG−SH@AuNPs	SPR peak (nm)	Hydrodynamic diameter (nm)	Zeta potential (mV)
IMC−PEG−SH@Au_{19}NPs	529	19.2 ± 0.2	−19.0
IMC−PEG−SH@Au_{33}NPs	542	33.4 ± 0.3	−23.5
IMC−PEG−SH@Au_{64}NPs	556	64.3 ± 0.2	−33.0

^{1}H NMR and ^{13}C NMR of compound（1）

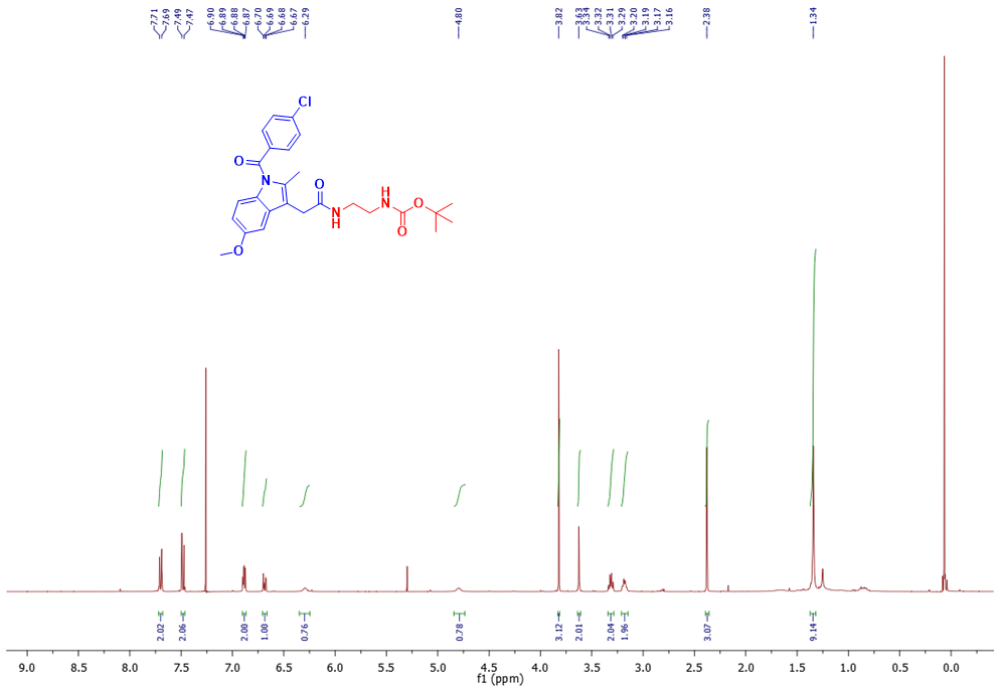

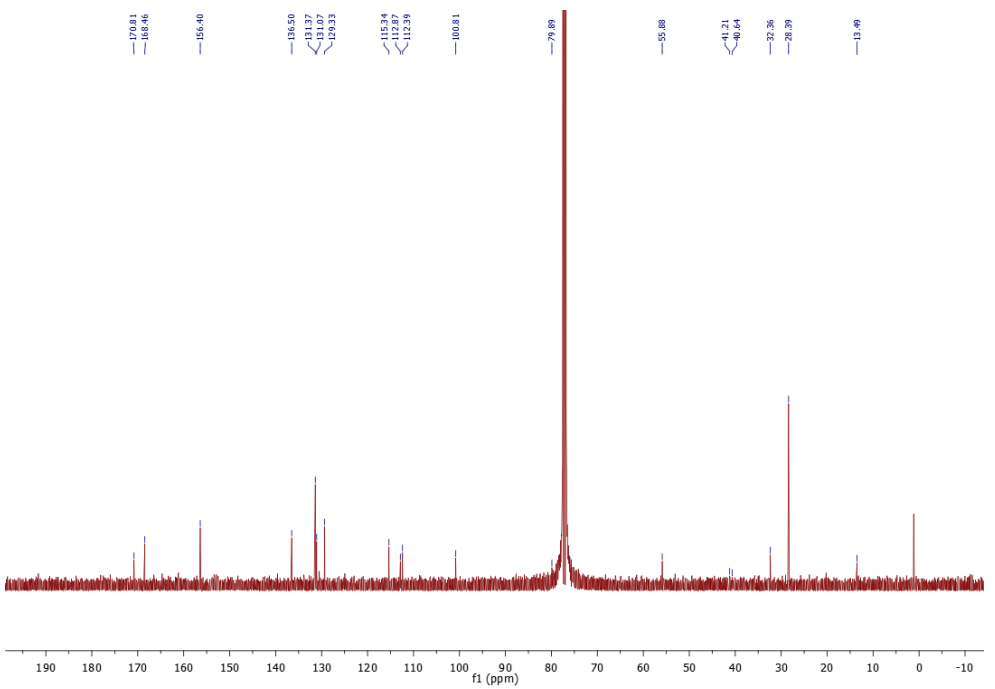

^{1}H NMR and ^{13}C NMR of compound（2）

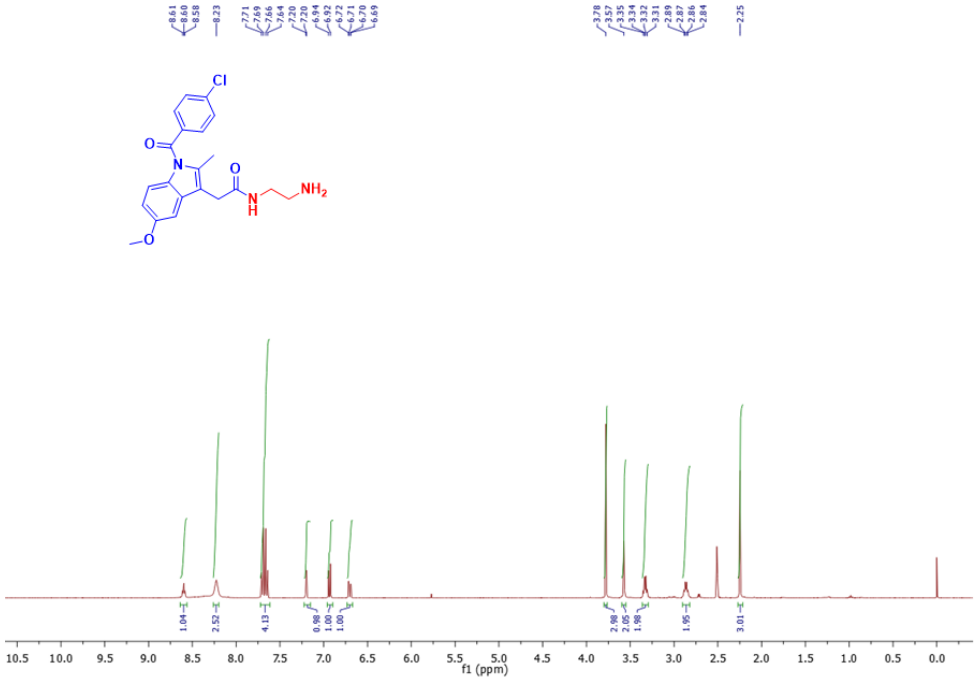

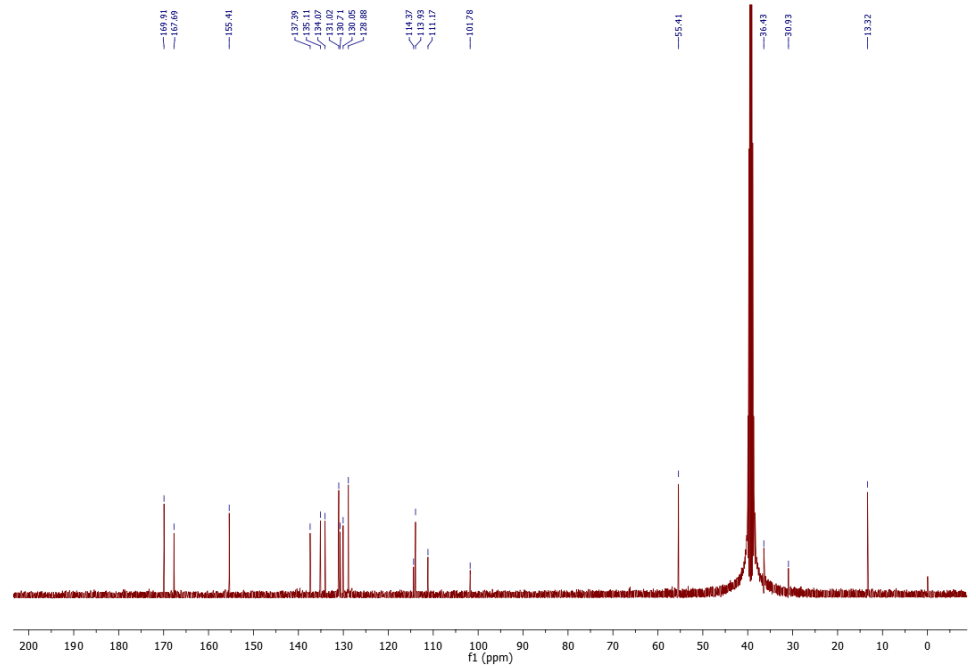

^{1}H NMR and ^{13}C NMR of compound（3）

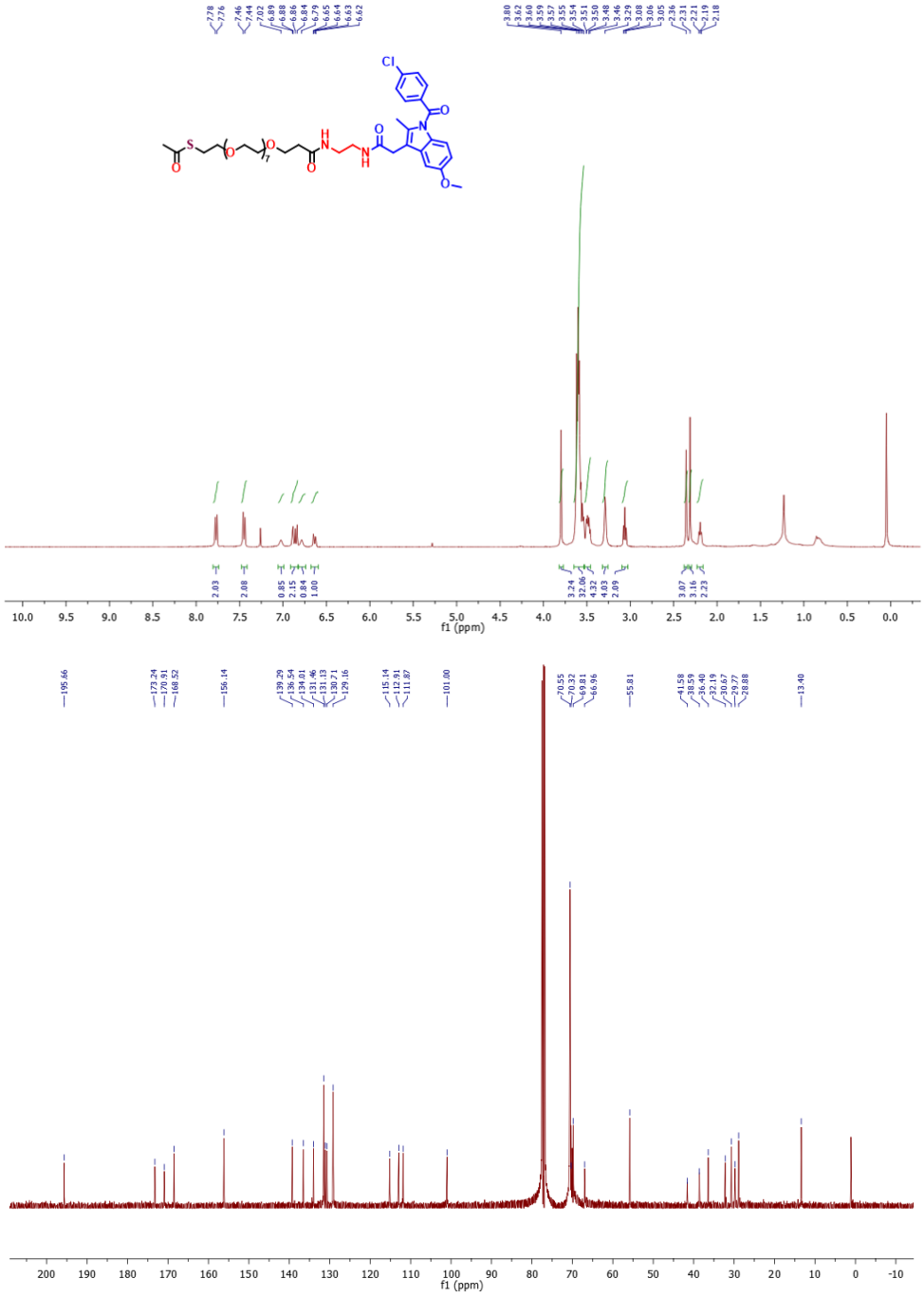

^{1}H NMR and ^{13}C NMR of compound（4）

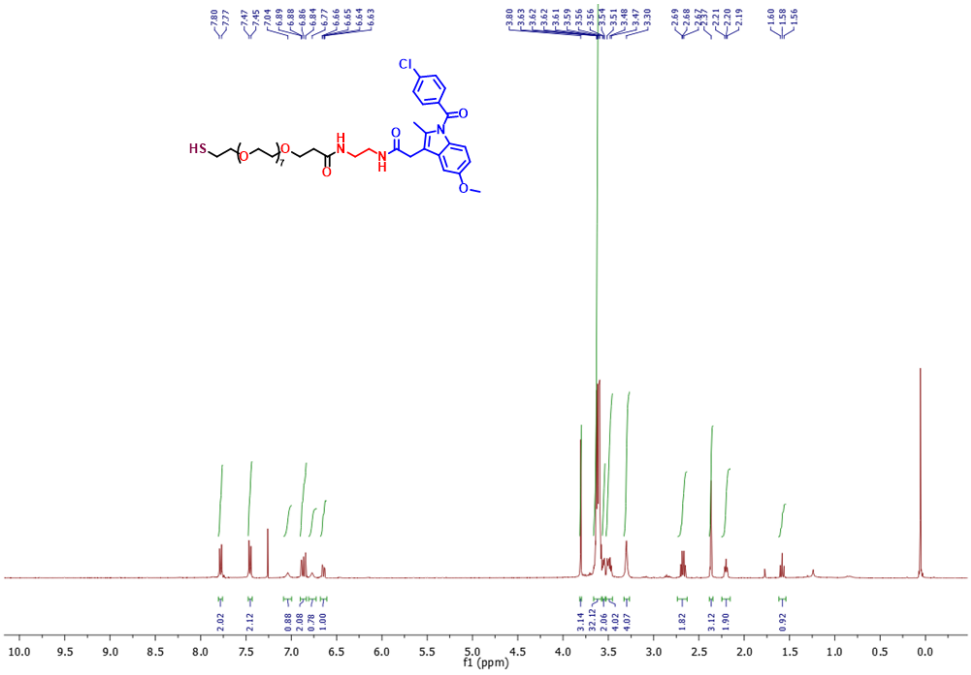

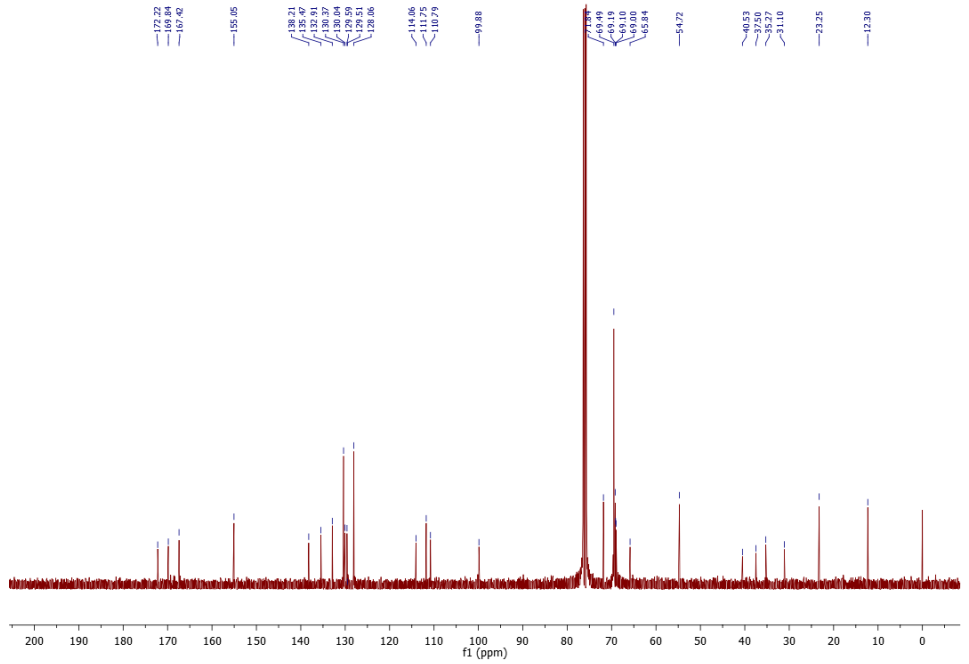

^{1}H NMR and ^{13}C NMR of compound（6）

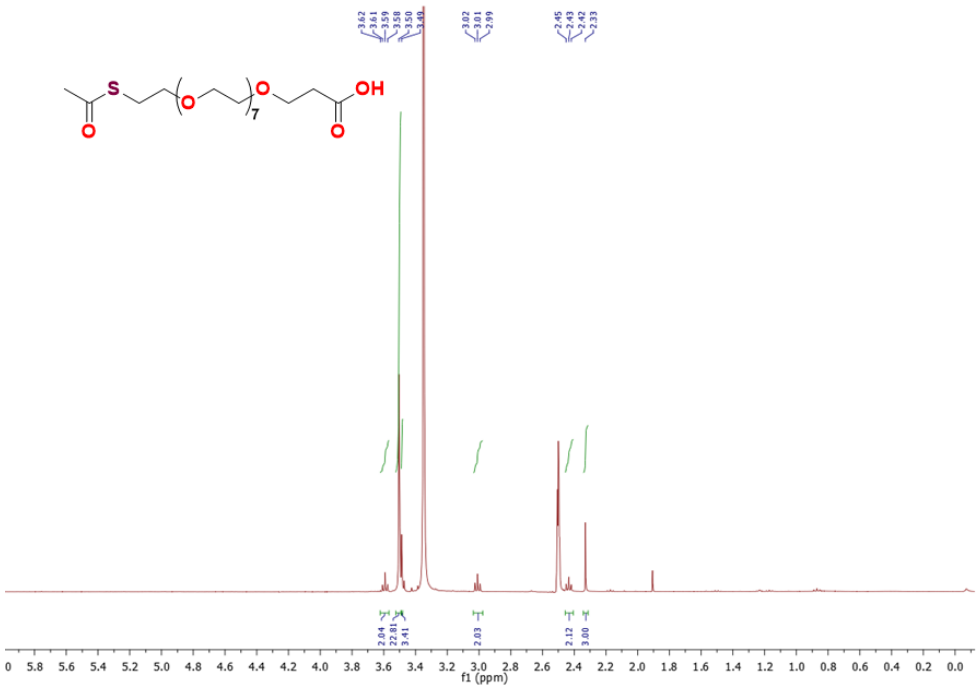

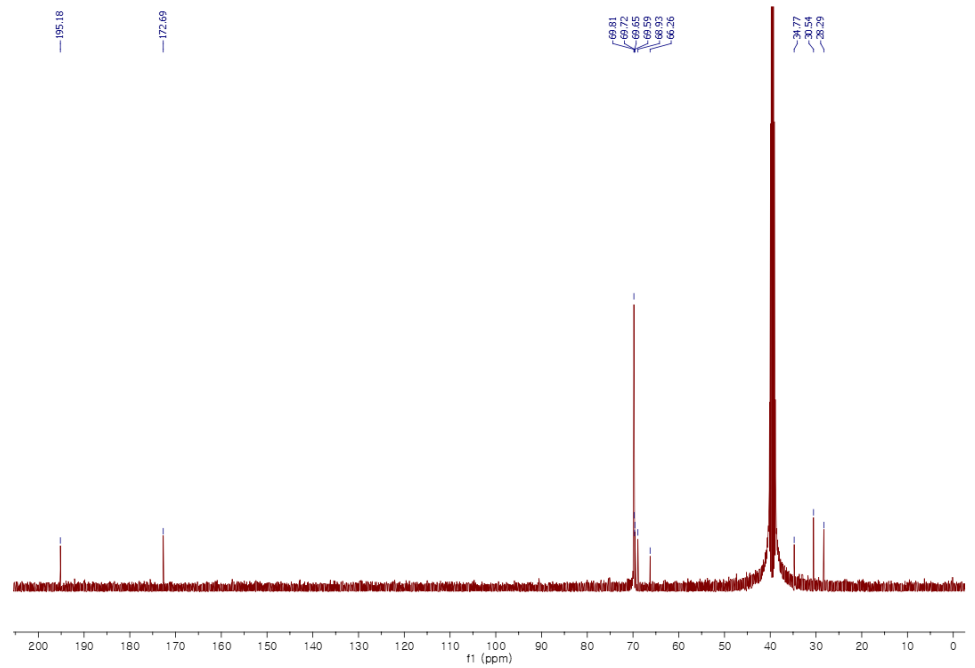

HRMS analysis of compound（4）

Qualitative Compound Report

Data File	SGB-116_1.d	**Sample Name**	SGB-116
Sample Type	Sample	**Position**	Vial 1
Instrument Name	Instrument 1	**User Name**	6530-PC\admin
Acq Method	DIP method-0p.m	**Acquired Time**	12/15/2021 6:09:05 PM
IRM Calibration Status	Success	**DA Method**	Default.m
Comment			
Sample Group		**Info.**	
Stream Name	LC 1		

Compound Table

Compound Label	RT	Mass	Abund	Formula	Tgt Mass	Diff (ppm)
Cpd 1: C40H58ClN3O12S	0.186	839.3415	164533	C40H58ClN3O12S	839.343	-1.71

Compound Label	RT	Algorithm	Mass
Cpd 1: C40H58ClN3O12S	0.186	Find By Formula	839.3415

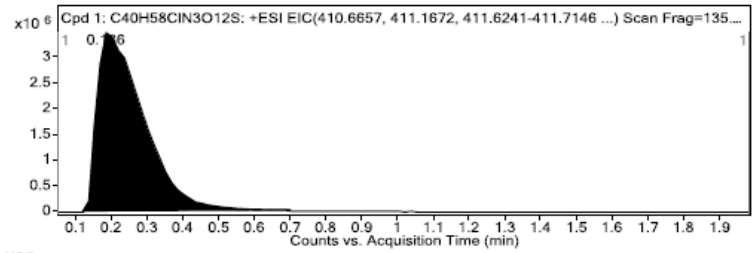

MS Spectrum

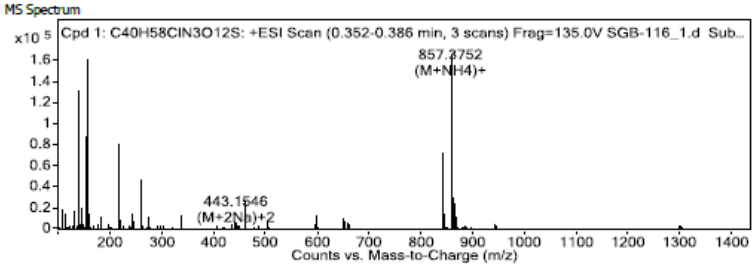

Qualitative Compound Report

MS Zoomed Spectrum

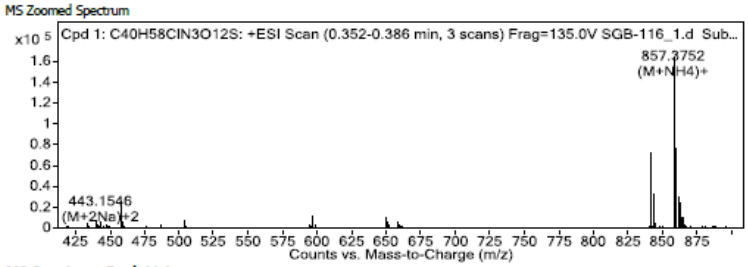

MS Spectrum Peak List

m/z	*Calc m/z*	Diff(ppm)	z	Abund	Formula	Ion
442.6466	442.6607	-31.82	2	253	C40 H58 Cl N3 Na2 O12 S	(M+2Na)+2
839.3451	839.3424	3.13	1	1859	C40 H58 Cl N3 O12 S	M+
840.3489	840.3502	-1.59	1	72952	C40 H59 Cl N3 O12 S	(M+H)+
841.352	841.3534	-1.76	1	33333	C40 H59 Cl N3 O12 S	(M+H)+
842.3491	842.3495	-0.52	1	33908	C40 H59 Cl N3 O12 S	(M+H)+
857.3752	857.3768	-1.91		164533	C40 H62 Cl N4 O12 S	(M+NH4)+
858.3794	858.3799	-0.61		74917	C40 H62 Cl N4 O12 S	(M+NH4)+
859.3754	859.3761	-0.84		76790	C40 H62 Cl N4 O12 S	(M+NH4)+
862.335	862.3322	3.29		25046	C40 H58 Cl N3 Na O12 S	(M+Na)+
878.307	878.3061	1.02	1	1582	C40 H58 Cl K N3 O12 S	(M+K)+

--- End Of Report ---